

Lars Thoresen Haug

Hydrodynamic Study of ROV (Remotely Operated Vehicle) Operations at Net-based Fish Farms

Masteroppgave i Marine Technology

Veileder: Marilena Greco

September 2020

NTNU
Norges teknisk-naturvitenskapelige universitet
Fakultet for ingeniørvitenskap
Institutt for marin teknikk

Lars Thoresen Haug

Hydrodynamic Study of ROV (Remotely Operated Vehicle) Operations at Net-based Fish Farms

Masteroppgave i Marine Technology

Veileder: Marilena Greco

September 2020

Norges teknisk-naturvitenskapelige universitet

Fakultet for ingeniørvitenskap

Institutt for marin teknikk



Kunnskap for en bedre verden

Summary

There is a tendency of aquaculture moving farming locations to increasingly exposed locations. At the same time, the industry are facing problems with rupture of net structures and consequently fish escapes. Development of Remote Operated Vehicles (ROVs) recent years has been a part of automation of the industry. This allows for a relatively cost efficient way of inspecting nets and thereby prevent ruptures before they becomes to large. For ROVs to function at more exposed locations it is necessary to understand how the flow of the water behaves around a fish farm when waves and currents are stronger.

Weather data from one of SINTEFs aquaculture locations at Tristeinen is analyzed to better understand important factors in modelling of the environmental loads. This is used as reference for creating a wave spectrum and velocity profile for the simulations. The target is to find a sea condition close to the operational limit of the ROV. Two spectra are created from a swell - and wind dominated seastate.

Modeling of the environmental loads are performed by creating a random time realization from the spectra. Every simulation is done with the same phase angle for consistency. The model of the net cage system is obtained from SINTEF, but it was necessary to create a routine for automatically generate mesh based on the resolution. A numerical convergence study was conducted on the fish cage system to identify the discretization error.

, an assessment on the net wake effect on the ROV is conducted. The sum of cylinder model will be analyzed for individual screens and later implemented into a program for calculating the velocity around a 2D net cage subjected to a uniform flow. A MATLAB program is made to develop and test the model against experimental results. Later a subroutine will be written into the source code of FhSim, the simulation software of SINTEF.

At last, time domain simulations of the ROV trajectories during 4 different "missions" will be conducted.

Preface

The master thesis was written as the final grade of a Master's degree at the Norwegian University of Science (NTNU) in 2020. The topic of the thesis evolves around modelling of fish cage structures, hydrodynamic response and ROV control systems. I was unfamiliar with most of the methodology used for simulations of aqua-cultural systems prior to the work. With excellent guidance from my supervisor at NTNU prof. Marilena Greco I was pointed in the right direction from the beginning, when exploring ways of improving existing calculation methods of the flow around a net cage structure.

The thesis was written during the outbreak of the COVID-19 pandemic which provided some additional challenges with supervising from NTNU and SINTEF. I am very impressed of how flexible prof. Marilena Greco and co-supervisor Walter Caharija has been when conducting meetings over video conference software. I also want to give a special thanks to Biao Su at SINTEF, whom essentially acted as an additional supervisor for me.

Lastly, I must give an huge gratitude to my girlfriend who has held the family under control during the most intense periods.

Table of Contents

Summary	1
Preface	2
Table of Contents	4
List of Tables	5
List of Figures	8
Nomenclature	9
1 Introduction	11
1.1 Background and motivation	11
1.2 Problem Statement	12
1.3 Project Thesis	12
2 Assessment of Environmental Loads During ROV Operations	15
2.1 Wind	15
2.2 Waves	15
2.3 Current	16
3 Numerical Model Framework	19
3.1 Modelling of Environmental Loads	19
3.1.1 Wave Field	19
3.1.2 Current	20
3.2 Modelling of Fish Farm system	22
3.2.1 Net Cage	23
3.2.2 Floating Collar	25
3.2.3 Bottom Ring	26
3.2.4 Mooring system	26
3.3 Modeling of Remote Operated Vehicle	27
3.3.1 Definition of Coordinate Systems	28
3.3.2 Hydrostatic Forces	28
3.3.3 Hydrodynamic Forces	29

3.3.4	Control System and Thruster Forces	30
3.3.5	Note on Model Assumptions and Limitations	30
4	Numerical Convergence Study on Net Mesh	31
4.1	Current only	31
4.2	Alligned Waves and Current	32
5	Assesement of net wake effect on ROV	35
5.1	Wake Behind Screens	35
5.1.1	Lølands Formula	35
5.1.2	Sum of Cylinders model	36
5.1.3	Plane turbulent mixing	38
5.2	Flow through and around cage	38
5.2.1	Wake Model Methodology	38
5.2.2	Wake Model Comparison With Experiments	44
6	Time Domain Simulations of ROV Trajectory	45
6.1	ROV Response Around a Rigid Net	46
6.1.1	Mission Number 1	46
6.1.2	Mission Number 2	47
6.1.3	Mission Number 3	48
6.1.4	ROV Response Sensitivity to Sea Condition	49
6.2	ROV Response Around a Moored Fish Cage	49
6.2.1	Mission Number 1	49
6.2.2	Mission Number 2	50
6.2.3	Mission Number 3	50
6.2.4	Mission Number 4	50
6.3	ROV Response Around a Moored Fish Cage Including the Wake Model	51
6.3.1	Mission Number 4	51
7	Conclusion	53
7.1	Environmental Loads	53
7.2	Wake Model	53
7.3	Time Domain Simulations	53
7.4	Recommendations for further work	54
	Bibliography	54
	Appendix	57
7.5	Net Mesh Creator in MALAB	57
7.6	ROV Properties and Parameters	57
7.7	Wake Model in MATLAB	58

List of Tables

2.1	Mean current velocity probability of exceedance	17
3.1	Discretization error on the estimation of significant wave height H_S	20
3.2	Validity range of force model	25
3.3	Floating collar dimensions	26
6.1	Initial position parameters	46

List of Figures

1.1	ROV prototype	12
2.1	Torsethaugen Spectra	16
2.2	Mean current from all depths	17
2.3	Change of Current Directions	18
2.4	Standard Deviation of Current Direction in Each Depth Layer	18
3.1	Discretization of Torsethaugen Spectra	20
3.2	Velocity Profile	21
3.3	Fish farm system components	22
3.4	Force components on panel	24
3.5	Rov visualtization in FhSim	27
3.6	Thruster positions and attitudes	27
3.7	ROV Gravity Forces Kinematics	28
3.8	Thruster curve	30
4.1	Net mesh divided in sections	32
4.2	Mean anchor forces (a), and mean drag forces (b) with increasing mesh refinement.	32
4.3	Relative anchor forces difference (a), and relative drag forces difference (b) with increasing mesh refinement.	33
4.4	Mean anchor forces (a), and mean drag forces (b) with increasing mesh refinement.	33
4.5	Relative anchor forces difference (a), and relative drag forces difference (b) with increasing mesh refinement.	33
5.1	Sum of Cylinder model diagram	37
5.2	Velocity contours of the reduced velocity for two screen configurations	37
5.3	Diagram of plane mixing layer between two separated flows	38
5.4	Schematic of cylinder cross flow	39
5.5	FhSim Wake Model Flow Chart	40
5.6	Stream lines and velocity vector plot of cylinder cross flow	42
5.7	Velocity contour plots of cylinder cross flow	43
5.8	Comparison between wake model and experimental data	44
6.1	Schematic of setup for the simulated missions	45

6.2	Results from mission number 1 around a rigid net	46
6.3	Results from mission number 2 around a rigid net	47
6.4	Results from mission number 3 around a rigid net	48
6.5	Results from mission number 1 with fish cage.	49
6.6	Results from mission number 2 with fish cage.	50
6.7	Results from mission number 3 with fish cage.	50
6.8	Results from mission number 4 with fish cage.	51
6.9	Results from mission number 4 with fish cage and wake model.	51

Nomenclature

Symbols are ordered alphabetically. Some symbols have multiple uses.

a_i	Nodal acceleration
C_A	Coriolis-centripetal matrix due to added mass
C_D	Drag force coefficient
C_L	Lift force coefficient
C_N	Normal force coefficient
C_{RB}	Rigid Body Coriolis-centripetal matrix
C_T	Tangential force coefficient
D	Damping matrix
u	Current velocity
d	Twine diameter
F_D	Drag force
F_L	Lift force
F_N	Normal force
F_T	Tangential force
H_S	Significant wave height
H_{m0}	Zereth moment (approx. to significant wave height)
k	Wave number
m_i	Nodal mass
M_A	Added mass matrix
M_{RB}	Rigid body mass matrix
t	Time
Re	Reynolds number
Sn	Solidity ratio
T_P	Peak frequency
T_f	Spectral peak frequency (double peaked spectrum)
ϵ	Relative error, virtual kinematic viscosity
λ	Mesh size
ω	Circular frequency
θ	Phase angle of wave, roll angle
ζ_A	Wave amplitude
ζ	Wave elevation

Introduction

1.1 Background and motivation

Net-Based fish farms are the most common design type for farming of Atlantic salmon in Norway. Although development of semi-closed and closed fish farms are making progress, this technology is still premature for the large proportion of the market. The economic benefits of utilising natural wave- and current energy for fresh oxygen supply to the abiotic environment gives the net-based fish farm a competitive advantage over other design types. It is therefore expected that net-based fish farms will still be the dominant design type in the industry for many years to come.

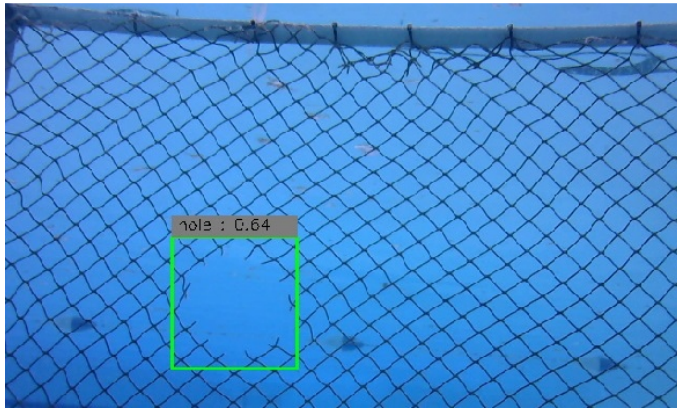
Fish farms are produced in different geometrical forms, depending on the requirement of withstanding environmental loads. For weather exposed locations, typically a cylindrical shaped cage is used. This is the type of design which will be investigated in this study.

One of the main challenges with the net-based fish farm is escapes of fish. This is in most cases caused by ruptures in the net. The industry has incentives to reduce the number of fish escapes from a couple of reasons. One is the direct impact on the loss of production, the other is restriction being made on future production in the area from authorities. Due to the alleged negative impact farmed salmon has on wild salmon, The Directorate of Fisheries may withdraw production licenses if a certain escape threshold is reached. Even though there is a discussion on how large the environmental impact really is from fish escapes, this problem has caused restrictions on existing aquaculture locations.

A part of the solution to the problem of net rupture is to frequently perform inspections and repairs on the net. Historically, this is manually done by human divers, which is relatively costly and unfeasible to do at a frequent level. The introduction of Remotely Operated Vehicles (ROVs), these operations can be performed at a much higher rate.

ROVs are submerged vessels, typically powered through an umbilical and controlled from surface. The often box like design makes it unfitting for high velocity operations, but is very suitable for mounting instruments. In the industry today, most ROVs have cameras installed for inspections of the net. Future instrument technology is also aiming at being able to perform repairs of the net, without the need of manual labor.

In recent years, new fish farm installations are located at increasingly exposed locations. Lack of available room in sheltered areas along the coast of Norway and the introduction of large scale ocean based fish farms, forces new projects out towards the ocean. In these conditions, navigation of ROVs can be very difficult due to the large motions caused by waves and current forces. To create a control system that is able to navigate and keep the ROV in an upright position when affected by large environmental loads, it is essential to fully understand the interaction between the vessel and the net.



(a) Photo of a detected hole in a fish cage net (ocean.gatech.edu)



(b) Prototype of ROV for net repairs (Sintef.no)

Figure 1.1

1.2 Problem Statement

In this thesis we will study a ROV operating close to the operational limit around a net-based fish farm. It is desirable to model the environmental loads, i.e waves and current, as realistic as possible. Therefore, weather data from a fish farm site will be used to construct a current profile and wave spectra. Further, a model of a fish farm system is to be created, including mooring, net, floating collar and a bottom collar. A model of the ROV includes a motion control system and a force model (hydrodynamic loads).

An in-house SINTEF software called FhSim will be used to do the simulations. The current version of the program does not account for the wake effect downstream of the net. Therefore, current velocities will be overestimated on the backside of the net, relative to the current direction. In this thesis, a 2D wake model will be developed, that calculates the reduced velocity in the wake.

By simulating different "missions" (navigation trajectories), we will investigate the following:

1. Test sensitivity of environmental loads on positional parameters and thruster forces during ROV mission trajectories.
2. Test sensitivity of "wake model" on positional parameters and thruster forces during ROV mission trajectories.

1.3 Project Thesis

In preparation of the master thesis the project thesis was exploring a number of problems regarding modelling of disturbance around a conventional fish cage. Initially, relevant environmental conditions had to be decided to use in the following simulations.

It was decided that different trajectories of the ROV were to be tested in the most extreme operational conditions. This does not include general extreme weather at the aquaculture location, such as autumn storms or similar. Rather, an extreme 1h seastate within a data-collection period of 3 months from march to end of may. Weather data from Tristeinen, one of SINTEF's aquacultural location at the coast of Trøndelag was collected. This is a semi-exposed location, meaning that there are several open sectors in most directions for development of wind generated waves, as well as incoming swell waves from the ocean.

It was found from the weather data that in general two types of seastates can be identified with regards to wave energy; swell dominated sea and wind dominated sea. Two doubled peaked spectra was developed in order to simulate the two different conditions.

Assessment of Environmental Loads During ROV Operations

Numerous studies have been done by investigating the response of a fish farm system in under different environmental loads. Although, no studies known to the author performs simulations under wave and current loads from real locations. In this chapter, analysis of weather data from a SINTEF owned fish-farm location at the coast of Trøndelag in Norway will be presented. The target is to find a sea condition which is close to the operational limit of the ROV. Notably, there were no large storm events during the data collection period.

2.1 Wind

The wind loads are assumed not important for the motion of the fish farm, thus not affecting the relative motion between the ROV and the not.

The wind data can however give a good indication of the direction and magnitude of wind generated waves. It can be seen in figure ??a that the north and west are the main wind directions. The wind from north has in most cases a velocity between 0 and 4 m/s, thus we can define the wind from west as the predominant wind direction as the wind velocity from this direction often exceeds 8 m/s.

2.2 Waves

It is expected that the location will experience both swell waves and wind waves. Swell waves are generated in wind events far away and contains a higher density of low frequency wave components, as the high frequency components is dissipated before reaching the location. The wind waves are generated locally by wind, thus containing higher frequency components than the swell waves Lader et al. (2017).

The wave data of the sample contains the significant wave heights H_s , maximum wave height H_{max} and the peak period T_p of each 1-hour sea state. Since we are interesting in a sea state that is close to the operational limit of the ROV, we will look at sea states where H_s exceeds 1.6 m to determine the design spectra.

Analysis of the data shows that there are two sea types that occurs in the time period of the data collection, for $H_s > 1.6m$. Some sea states are dominated by wind generated waves, meaning that the peak period from the sample data $T_p < T_f$. Other samples of the data shows a swell dominated sea state where $T_p > T_f$. T_f is the limit of locally fully developed sea and is defined from empirical studies by the following equation (Torsethaugen et al. (2004)).

$$T_f = a_f H_s^{1/3} \quad (2.1)$$

The parameter $a_f = 6.6$ is assuming fetch length of 370 km. The model used to establish the spectra is the simplified Torsethaugen spectra, which is essentially two superimposed JONSWAP spectra of swell and wind waves as described in Torsethaugen et al. (2004). For the wind dominated case we will have two peaks, while the spectra of swell dominated sea will have only one clear peak.

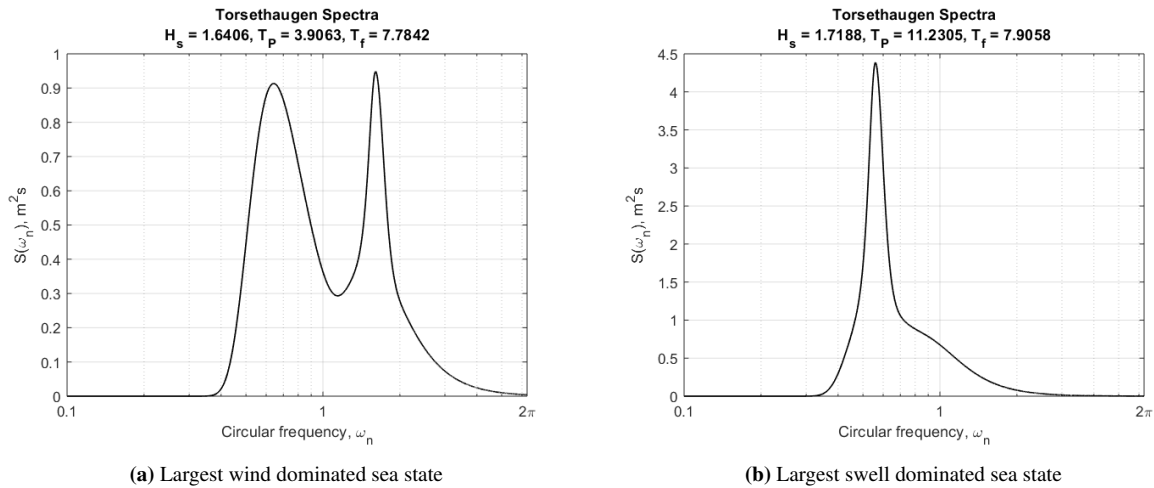


Figure 2.1: Simplified Torsethaugen Spectra.

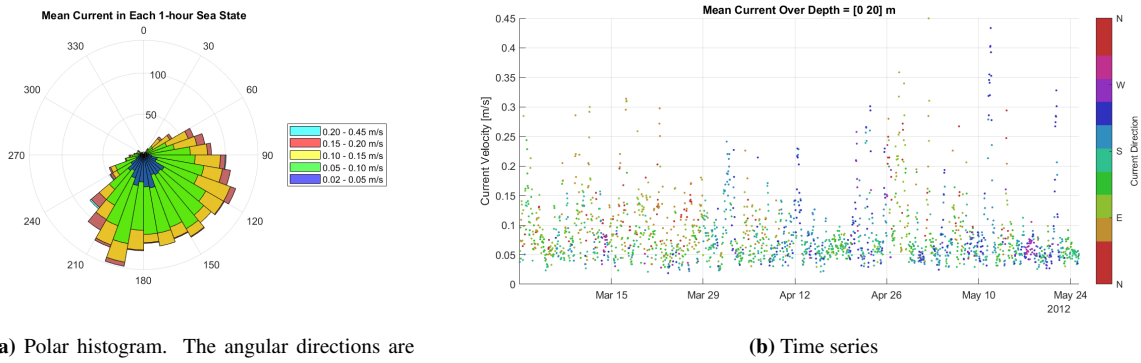
The model described should be interpreted with a caveat that it might overestimate the spectral energy at location relevant for aquaculture. Firstly, the assumed fetch length, which is the distance the wind generated waves can develop, might be significantly lower than the assumed distance of 370 km. Typically this is the case if the location is sheltered from open waters. At Tristeinen it is unclear if the small islands surrounding the location are large enough to reduce the fetch length. A lower fetch length reduces the amount of high frequency waves in the spectrum. Secondly, the Torsethaugen Spectra was developed for open waters. Areas surrounding the fish farm might be relatively shallow, thus some of the wave energy is dissipated.

2.3 Current

The development of Ocean currents are caused by a number of far away and local events. Differences in temperature and salinity in the ocean cause mass flow of water, while wind generate a boundary layer from the surface. For this location, the most influencing factor is assumed to be local wind events. Also, tidal variations cause large mass flow of water in inlets to fjords or similar, causing the effect of a funnel. Although, in the measuring period, data from Kartverket shows that the maximum variation between spring tide and neap tide is of only 0.94 m. This suggests that this effect is of minor importance for this area.

Data is collected from 20 depth ranges of 2 m, making the total measuring depth of 40 m. Although, here we will present mean values over the range 0-20 m depth, since this is the most relevant range for ROV operations. At this location, the current is strongest near the surface and gradually becomes weaker at 20 m depth. To give an impression of the currents at Tristeinen, the mean value from water depth 0-20 m are plotted as a polar histogram and a time series as can be seen in Figure 2.2 a and b.

Most of the time, the currents are relatively small in magnitude, ranging from 0.02-0.1 m/s. This interval is classified by Norwegian Standard NS9415 (2009) as small exposure and is found present 74% of the time during the period of measurement. Currents classified as moderate exposure of 0.3 m/s is exceeded only about 1% of



(a) Polar histogram. The angular directions are relative to north = 0 deg.

(b) Time series

Figure 2.2: Mean current from all depths (0-20m) in the corresponding mean flow direction during the data collection period

the time. A list of probability of exceedance can be found in tab. 2.1 Even though these higher currents rarely occur in this measuring period, it is expected that higher velocities can occur in fall and winter due to higher wind velocities. Also, we can see from fig. 2.2 b) that the higher velocity events are clustered in the time series, meaning that there are periods where higher velocities might not be avoided for ROV operations.

Table 2.1: Mean current velocity probability of exceedance in measuring period

U [m/s]	0.05	0.10	0.15	0.20	0.25	0.30
P(u>U)	0.77	0.26	0.11	0.052	0.025	0.0093

The time series of the mean current velocities in fig 2.2 b) are also color coded with the mean current directions to visualize the change of current direction. Notably the current direction changes much from hour to hour in some periods, indicated by the large color difference in the scattered plot. This seems especially significant in March and May, which has an impact on the assumption of modelling of current with steady direction. To further investigate this, the change of mean current direction from the previous hour is plotted as can be seen in fig 2.4. The plot distinguishes the change of direction based on the mean velocity in three ranges: 0.02-0.1, 0.1-0.2 and 0.45 m/s. For the lower mean velocities the change of direction is very scattered and has a high chance of changing direction significantly each hour. It is assumed that the reason for this is that for the lower velocity ranges, less energy is required to change the momentum of the flow. Thus, modelling of a steady direction is inaccurate for low velocities. For the highest range, the distribution of the velocity changes are narrower as indicated in the probability density diagram to the right in fig 2.4. This means that modelling of a steady flow direction is assumed reasonable for the highest velocities.

It was also observed from the data the current direction in each depth layer had a large deviation from the mean direction for most values. This is important for the validity of a uniform current model. The standard deviation of each depth layer from the mean current direction is plotted in fig ???. The tendency is similar to the change of mean current direction; the flow direction is more uniform for higher velocities.

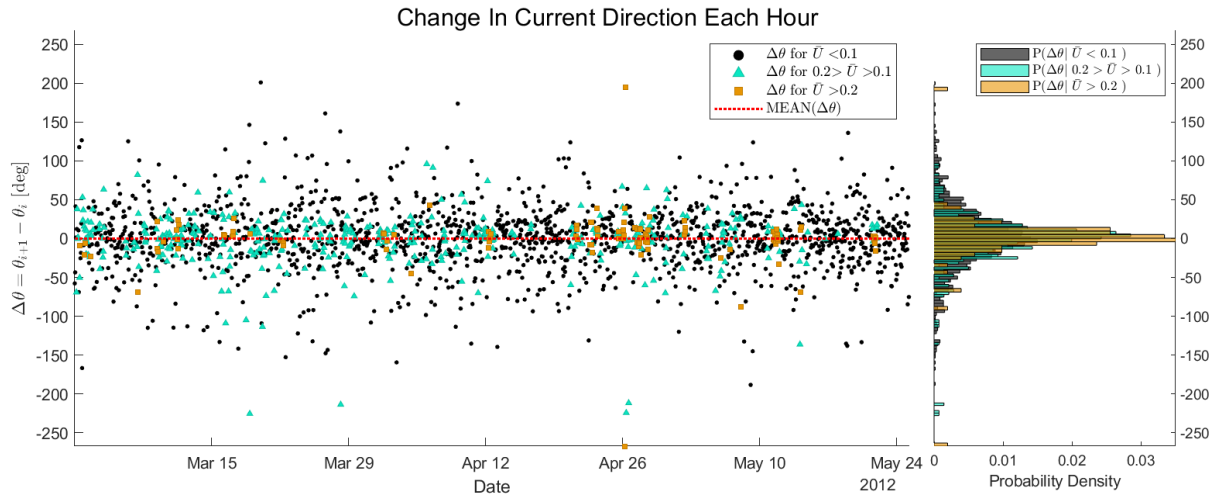


Figure 2.3: Change of Mean Current Directions. The symbol θ represent the mean current direction in depth range 0-20 m.

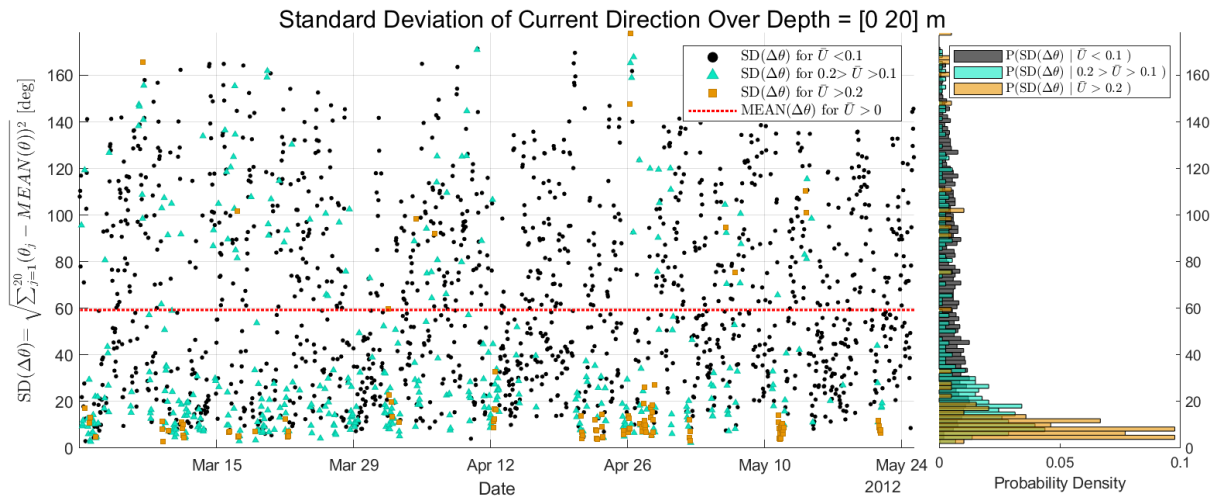


Figure 2.4: Standard Deviation of Current Direction in Each Depth Layer

Numerical Model Framework

3.1 Modelling of Environmental Loads

The fish cage system and the ROV will experience external loads from the environment. Loads from waves and current are considered to be of most importance. Wind loads do affect the surface piercing parts of the fish cage, although these loads are considered negligible to the response of the net. Wind loads are therefor not modelled in the simulations.

3.1.1 Wave Field

Modelling of irregular seastate is performed by summation of regular wave components, each with a different frequency, amplitude and phase.

The FhSim object used to model the sea environment is limited to 100 individual wave components as input to the program. The 100 corresponding wave amplitudes will be determined from the spectra by equation 3.1 for long crested waves.

$$\zeta_{A_n} = \sqrt{2S(\omega_n)\Delta\omega_n} \quad (3.1)$$

The wave components ζ_n will be defined by the amplitudes ζ_{A_n} , their corresponding frequencies ω_n and a uniform distributed random phase angle $0 < \theta_n < 2\pi$, such that

$$\zeta_n(x, t) = \zeta_{A_n} \cos(\omega_n t - k_n x + \theta_n) \quad (3.2)$$

, where x is the spatial position of the wave in the direction of propagation and $k_n = \frac{\omega_n^2}{g} \tanh(k_n h)$ is the wave number of each component for finite water depth.

The frequencies ω_n are distributed in a non-uniform way to capture the curvature of the spectra from the limited number of wave frequencies ω_n . In addition, the non-uniform distribution will avoid periodization of the time realization during the simulation period. The discretization of the spectra for the wind dominated sea state and the swell dominated sea are shown in figure 3.1.

The blue asterisk markers represent the 101 discretized points at the spectra. The $S(\omega_n)\Delta\omega_n$ term in eq. 3.1 are found by approximating the area under each discretized interval. This is done by interpolating linearly between each discretized point. The light blue squares will therefore represent the term $S(\omega_n)\Delta\omega_n$.

The method is introducing a small error to the zeroth moment of the spectra. By approximating the significant wave height from the discretized spectra, we can compare the H_S from the fine discretization and the spectra using

32 and 100 points with eq. 3.3.

$$H_{m0} \approx 4 \sqrt{\sum_{i=1}^N S(\omega_n) \Delta\omega_n} \quad (3.3)$$

Table 3.1: Discretization error on the estimation of significant wave height H_S

Sea type	Discretization	H_S [m]	H_{m0} [m]	$\epsilon = \frac{H_{m0} - H_S}{H_S}$
Wind dominated	32 points	1.6406	1.6626	1.32 %
	100 points	1.6406	1.6501	0.58 %
Swell dominated	32 points	1.7188	1.7545	2.08 %
	100 points	1.7188	1.7424	1.37 %

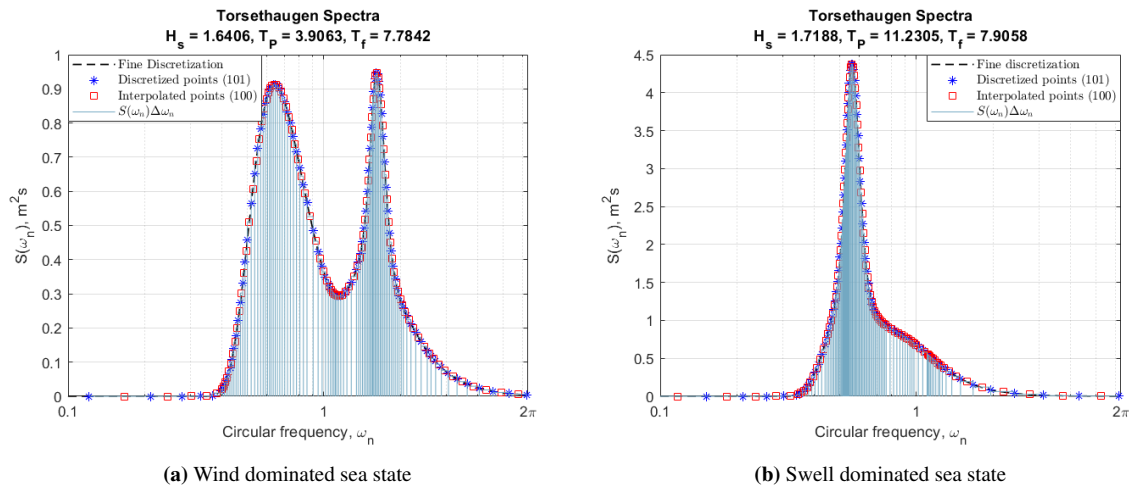


Figure 3.1: Simplified Torsethaugen Spectra. Frequencies used in the simulation are defined by the interpolated points (squares).

3.1.2 Current

The ambient current is modelled as a steady unidirectional flow aligned with the wave propagating direction. The flow has different velocities depending on depth. A velocity profile in lateral (z -direction) is given as an input to the program. The assumption of a unidirectional flow was found reasonable for large velocities as argued in sec 2.3. It is chosen to use a velocity profile from the same 1-hour sea state as the swell dominated waves for all simulations with current. This is done to make a better comparison between the different sea states, even though the velocity profile of the wind dominated sea state has a slightly higher mean velocity.

FhSim accepts an array of velocities in depth layers as input to the program as indicated in fig 3.2. The discontinuities between each depth layer are not considered important for the net force model, as the current force on each screen will be anyway distributed to a single node. As for the ROV, the discontinuities will cause a sudden change in velocity when moving from a depth layer to the next. However, it is assumed that the impact on the motion of the ROV is of minor importance.

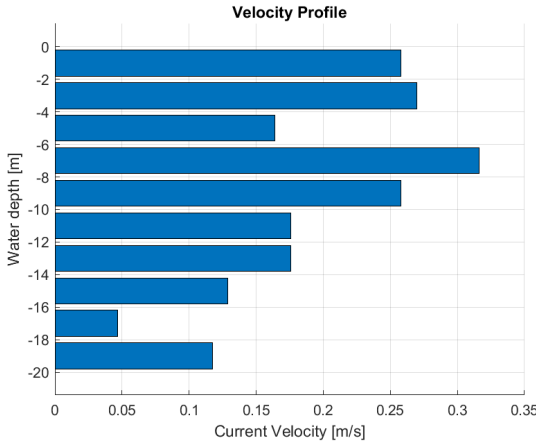


Figure 3.2: Velocity profile from measurements during the same time interval as for the largest swell dominated seastate.

3.2 Modelling of Fish Farm system

The cage and mooring system model was obtained from SINTEF, with its physical properties. It is an individual cage moored with tension cables in the floating collar and buoys. Usually a fish farm system is installed in arrays of $2 \times 6 - 10$ cages, although this individual model resembles the same properties as an array mooring arrangement. Since we are only investigating the interaction between the interaction between the ROV and the net at a single cage, computational time is saved. A schematic view of the components of the fish farm is shown in fig. 3.3.

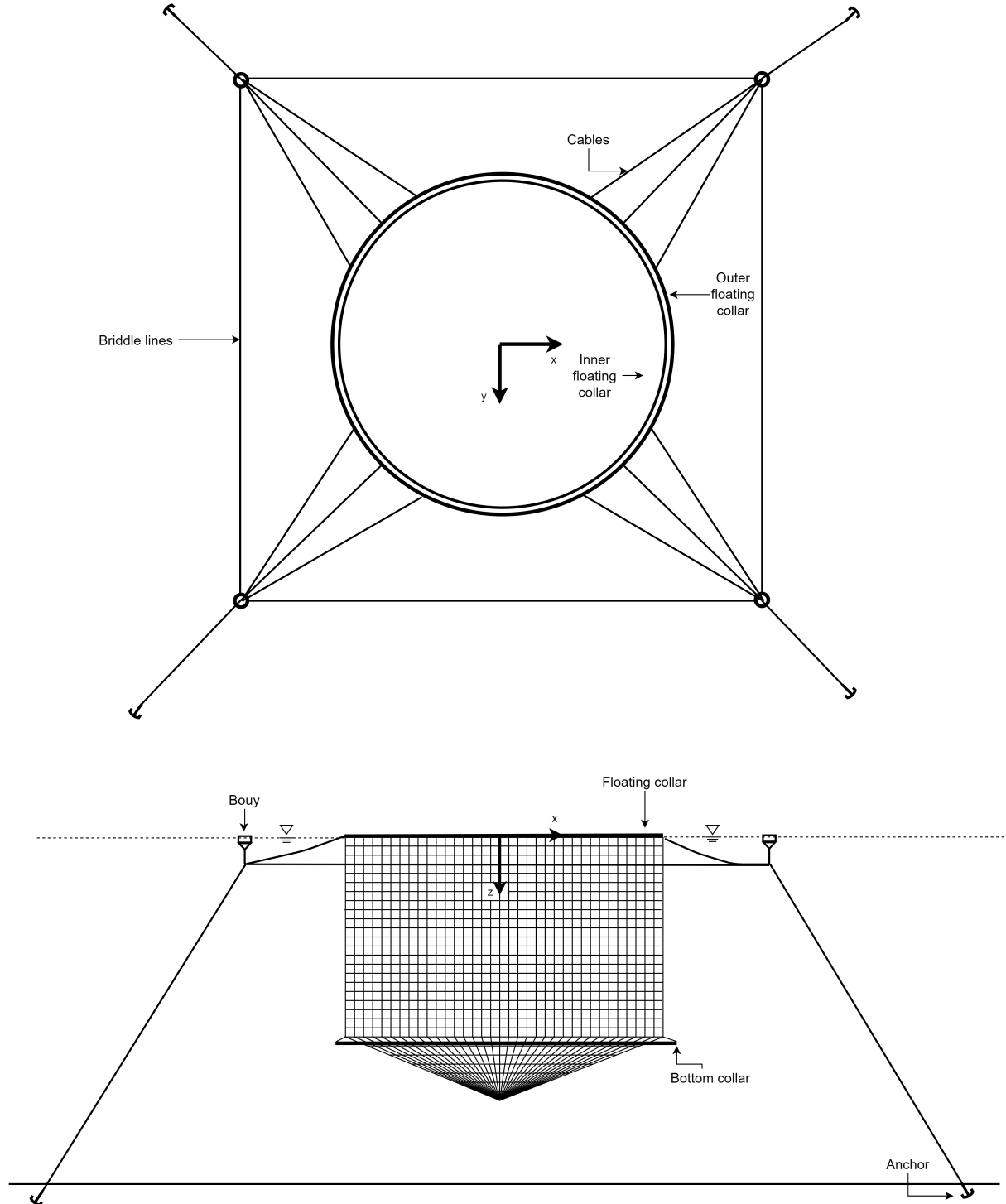


Figure 3.3: Fish farm system components

3.2.1 Net Cage

The net structure is discretized in a finite number of nodes and elements to represent the fine mesh structure of a net. A net typically consists of $\mathcal{O}(10^6)$ twines, which is unpractical to perform numerical calculations on in a time marching procedure as in CFD methods. Instead, methods are developed to let an area of the mesh, referred to as a screen or a panel, be representable for the hydrodynamic forces acting on the twines dependent on the solidity ratio Sn , Reynolds number Re and inflow angle θ . The screen is connected to one or several nodes, depending on the discretization method. The response of the nodes are governed by the equation of motion.

In each time step nodal forces are calculated using newtons second law. The nodal acceleration in each time step a_i is found from eq. 3.4. Numerical integration of the nodal acceleration is applied to obtain the instantaneous velocity and position of each node.

$$m_i a_i = \sum F_i \quad (3.4)$$

The nodal force F_i is calculated by adding the contribution from a linear stiffness term acting due to elongation of trusses between nodes (F_T), hydrodynamic loads acting on the mesh panel ($F_D + F_L + F_a$) and external forces from floating collar and bottom ring F_E (see eq. 3.5). The hydrodynamic loads acting on the panels are distributed at the node connected to the panels.

$$\sum F_i = \sum_{i=0}^{nnode} (F_T + F_D + F_L - F_a + F_E) \quad (3.5)$$

Triangular elements

Triangular elements are created from a nodal map. This is done by first discretize the net structure in a desired resolution $N_r \times N_v$, i.e number of nodes circumventing the structure and number of vertical nodes. In principal, the spacing between each node can take any value, however in this report the nodes has been consistently distributed uniformly.

A routine is made in MATLAB to automatically create a file mapping all the nodes, depending on the mesh resolution (see appendix 7.5.)

Viscous Loads

The calculation of viscous forces (drag/lift) are assuming a knotless net, with arbitrary shape (only dependent on Sn). The viscous loads are expressed as a function of the solidity ratio Sn , the non-dimensionalized water velocity Rn and the relative local inflow angle ϕ , which will be defined later.

The drag and lift forces are defined relative to incident velocity component as given in eq. 3.6 and 3.7. The following expression only include forces from vertical and horizontal mesh bars, thus knots are neglected.

$$F_D(Sn, Rn, \phi) = \frac{1}{2} \rho C_D A |U_{rel}| U_{rel} \quad (3.6)$$

$$F_L(Sn, Rn, \phi) = \frac{1}{2} \rho C_L A |U_{rel}| U_{rel} \quad (3.7)$$

, where A is the area of the panel. The relative velocity U_{rel} is defined by eq. 3.8 (Shen, 2018).

$$U_{rel} = rU_\infty + u_w - u_i \quad (3.8)$$

, where U_∞ is the ambient current velocity, u_w is the incident wave particle velocity and u_i is the nodal velocity.

The current reduction factor r is applied to all downstream panels, due to shading effect of current flow through upstream panels. The following expression of r is derived from experimental results by Løland (1991).

$$r = 1 - 0.46C_D^{(up)} \quad (3.9)$$

Here, the drag coefficient $C_D^{(up)}$ is given from the upstream panel that is shading the downstream panel in the direction of the ambient current.

The drag and lift coefficients are calculated from empirical formulas on cylinder cross-flow. The force coefficients are decomposed into a normal and tangential coefficient that is defined by the angle of the panel relative to the incident velocity α , as can be seen in fig. 3.4.

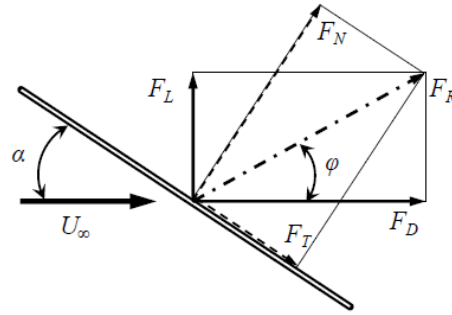


Figure 3.4: Decomposing of viscous forces acting on a panel. (Enerhaug et al., 2012)

The drag and lift force coefficients can be expressed in terms of a normal force - and tangential force coefficients (eq. 3.10 and 3.11).

$$C_D = C_N \cos \phi + C_T \sin \phi \quad (3.10)$$

$$C_L = C_N \sin \phi + C_T \cos \phi \quad (3.11)$$

The expression of the normal force coefficient C_N is assuming validity of cross-flow principle and is based on experimental data from Blevins (2003) and worked out by Kristiansen and Faltinsen (2012), as seen in eq. 3.12. This formulation is only valid for inflow angles ranging from 0-45°.

$$C_N(\phi) = \frac{C_D^{circ.cyl} S_n(2 - S_n)}{2(1 - S_n)^2} \quad 0 \leq \phi \leq \pi/4 \quad (3.12)$$

The expression for the drag coefficient around a circular cylinder is based on curve fitting of experimental data from Goldstein (1965).

$$\begin{aligned} C_D^{circ.cyl} = & -78.46675 + 254.73873(\log_{10} Re)^1 - 327.8864(\log_{10} Re)^2 \\ & + 223.64557(\log_{10} Re)^3 - 87.92234(\log_{10} Re)^4 + 20.00769(\log_{10} Re)^5 \\ & - 2.44894(\log_{10} Re)^6 + 0.12497(\log_{10} Re)^7 \end{aligned} \quad (3.13)$$

The tangential force is dependent on the normal force and is given in the following relationship.

$$\frac{C_T(\phi)}{\phi} = \frac{4C_N(\phi)}{8 + C_N(\phi)} \quad 0 \leq \phi \leq \pi/4 \quad (3.14)$$

The model of the normal force and tangential force may be extended to apply for all angles ϕ up to $\pi/2$ as described in Kristiansen and Faltinsen (2012).

The formulations of the force coefficients above are limited to the ranges specified in tab. 3.2.

Table 3.2: Validity range of force model

	Min	Max
Re	$10^{3/2}$	10^4
Sn	0	0.5

Added Mass Force

No documentation of the added mass term is found. However, it is assumed that the added mass on a net panel is connected to the disturbance caused by individual twines on the net. For a circular cylinder the added mass equals the water displaced (see e.g. Faltinsen (1993)). Assuming that strip theory is valid, i.e. the direction of the flow does not change on the twine, the added mass equals the displaced water by each of the cylinders. This gives the following expression of added mass on each node.

$$\frac{F_{a_i}}{N_n} = \rho_s \pi \frac{D_{tw}^2}{4} L_{tw} N_{tw} a_i \quad (3.15)$$

N_n : Number of nodes connected to element

ρ_s : Density of water

D_{tw} : Twine diameter

L_{tw} : Twine length

N_{tw} : Number of twines in element

a_i : Instantaneous nodal acceleration

Alternatively, one can assume that the net is buoyancy neutral, thus having the same mass as the displaced water. Then an approximation to the added mass force might be as follows.

$$F_{a_i} = m_i a_i \quad (3.16)$$

, where m_i is the lumped mass of the node.

External Forces

External forces from floating collar and bottom ring are added at connected relevant nodes.

3.2.2 Floating Collar

The floating collar is modeled as two circular flexible tori with 6 degrees of freedom. Euler-Bernoulli beam theory is used for calculation of elastic bending. Shear forces and torsion are neglected. The response is calculated using the modal superposition principle using 10 modes.

The dimension parameters of the floating collar are shown in Table 3.3.

Table 3.3: Floating collar dimensions

Diameter 1	Diameter 2	Mass	Torus Diameter	Elastic modulus
49.974706 m	50.9742 m	71.5423 kg/m	0.499746 m	$9 \cdot 10^8$ Pa

3.2.3 Bottom Ring

The bottom ring is modelled as cable elements with a high density and stiffness. The purpose of this sub-structure is to give a vertical force on the net to prevent it from drifting away with the waves and current.

3.2.4 Mooring system

The mooring arrangement consist of 12 bridle lines, 4 frame cables and 4 anchor lines interconnected to a connection plate under each of the four buoys. The connection plates is kept in place by a line to each buoy. Each line is modelled as a cable element.

3.3 Modeling of Remote Operated Vehicle

The model of the ROV is based on a Argus Mini (Argus, 2020) used for research purposes at SINTEF. Included in the simulations are calculations of the motion responses of the ROV in sea conditions. All models are attained from SINTEF and can in general be categorized as a hydrodynamic load - and control system model which will be briefly accounted for in the following sections. The following derivation of the ROV force model is obtained from Fossen (2011).

A generic visualization of the ROV is seen in fig. 3.5. The main dimensions of the vessel are $L \times B \times H = 0.90m \times 0.65m \times 0.50m$. Other ROV properties and calculation parameters are listed in Appendix 7.6.

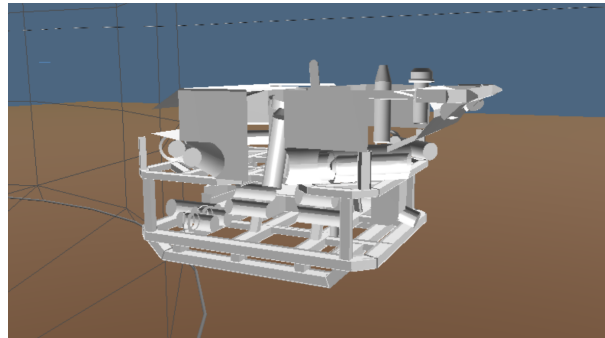


Figure 3.5: Rov visualization in FhSim

The propulsion system of the vessel consists of six thruster mounted symmetrically on the body as can be seen in fig. 3.6. Each is fixed in position and attitude, being able to control the motion in all six degrees of freedom. All thruster are able to apply force in both directions, which is dependent on the thruster curve.

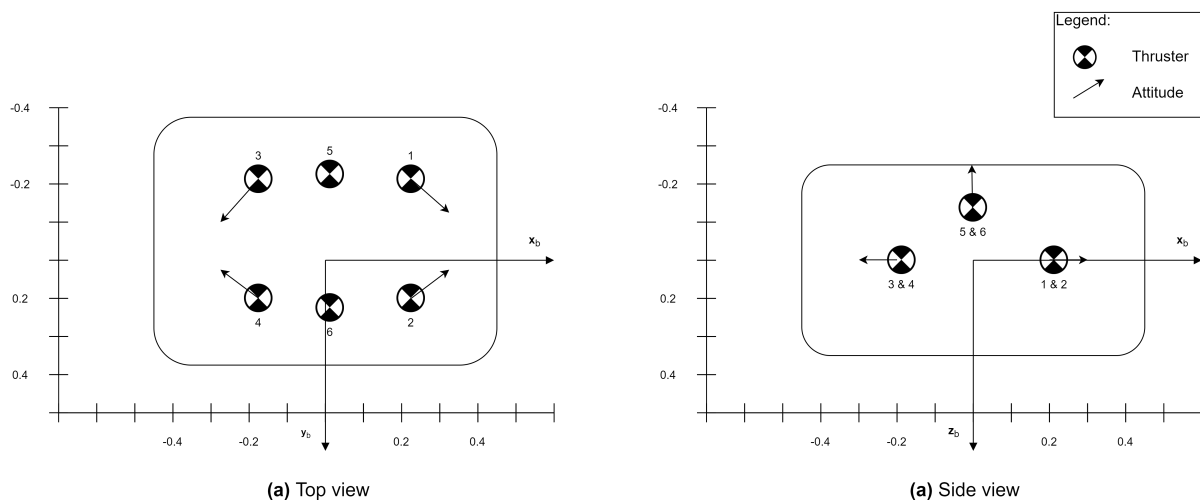


Figure 3.6: Thruster positions and attitudes

The response of the ROV is governed by the equation of motion (eq. 3.17) in six degrees of freedom (6 DOF). The instantaneous positions are found by time integration of Newtons second law.

$$\sum_{i=1}^6 \mathbf{F}_i = \mathbf{M}_{RB} \dot{\mathbf{v}}_i \quad (3.17)$$

The sub indices $i = [1, 2, \dots, 6]$ denotes the degree of freedom in surge, sway, heave, pitch, roll and yaw. Textbooks typically arrange the equation of motion such that external forces acting on the body are kept on the

right side. Here we will present the terms in a logical manner according to the solution strategy. The forces acting on the body can generally be divided into hydrodynamic -, hydrostatic - and thruster forces and moments.

$$\underbrace{C_{RB}(\nu)\nu}_{\text{rigid body}} + \underbrace{M_A\dot{\nu} + C_A(\nu_r)\nu_r + D(\nu_r)\nu_r - \tau_{wave}}_{\text{hydrodynamic}} + \underbrace{g(\eta)}_{\text{hydrostatic}} - \underbrace{\tau}_{\text{thruster}} = M_{RB}\dot{\nu} \quad (3.18)$$

Here, the rigid body terms are dependent on the velocities of the ROV ν , while the hydrodynamic forces are dependent on the relative velocity between the ROV and ocean currents:

$$\nu_r = \nu - \nu_c \quad (3.19)$$

The rigid body diagonal mass matrix is defined as follows:

$$M_{RB} = \text{diag}\{m \ m \ m \ I_x \ I_y \ I_z\} \quad (3.20)$$

Where m is the total body mass in kg and I_x , I_y and I_z are the moment of inertia about the axis of roll, pitch and yaw respectively.

3.3.1 Definition of Coordinate Systems

All previous and following equations in this section are defined in a BODY fixed frame. To retain compatibility between other objects, the velocity vector of the ROV ν , is transformed back to the earth fixed NED frame.

3.3.2 Hydrostatic Forces

The ROV is assumed submerged at all times, thus the magnitude of the buoyancy and gravity force vectors are constant at all times. Since orientation of the vessels changes during sea keeping, the components of the gravity force diagonal matrix changes with respect to the roll angle θ and the pitch angle ψ . The kinematics used for calculations of gravity and buoyancy forces are shown in fig. 3.7.

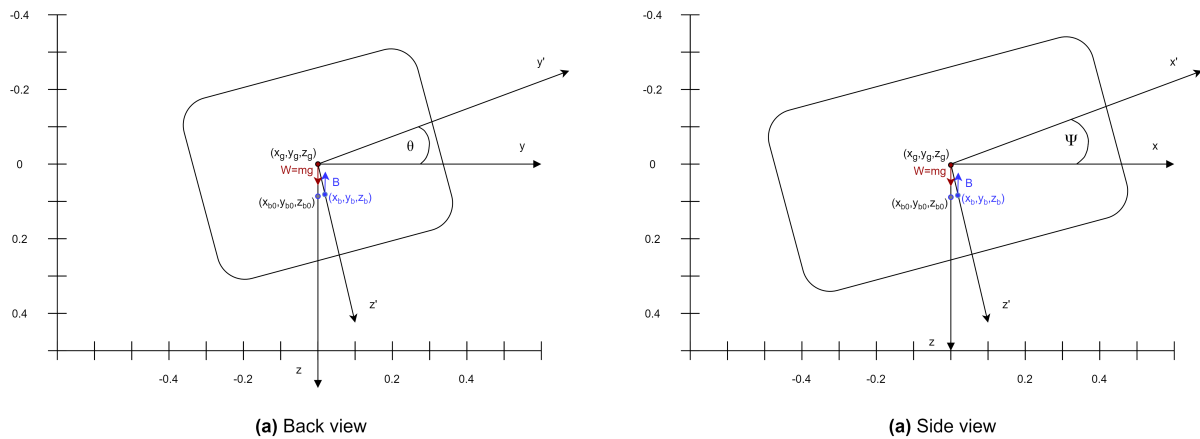


Figure 3.7: ROV Gravity Forces Kinematics

$$g(\eta) = \begin{bmatrix} (W - B) \sin(\theta) \\ -(W - B) \cos(\theta) \sin(\psi) \\ -(W - B) \cos(\theta) \cos(\psi) \\ y_{b0} B \cos(\theta) \cos(\psi) - z_{b0} B \cos(\theta) \sin(\psi) \\ -z_{b0} B \sin(\theta) - x_{b0} B \cos(\theta) \cos(\psi) \\ x_{b0} B \cos(\theta) \sin(\psi) + y_{b0} B \sin(\theta) \end{bmatrix} \quad (3.21)$$

3.3.3 Hydrodynamic Forces

The hydrodynamic forces are normally subdivided into two problems (see e.g (Faltinsen, 1993, p. 39)); *added mass* -, *damping and restoring terms* and *wave excitation loads*. The restoring terms are dealt with in the previous section and do not have any dependencies on the positional changes of the vessel, other than the attitude vectors.

Added Mass and Damping

The added mass and damping terms are the forces acting on the body, when the ROV is forced to oscillate (in 6 DOF) in still water. This means that the added mass - and damping coefficient has in reality a dependency on the frequency of the forced oscillation. Obtaining the most accurate description requires to solve this problem for the frequency of every incoming wave component. In the FhSim model, the long wave approximation is used, meaning that the coefficients are found from the limit where $\omega \rightarrow 0$. This saves computational time at each time iteration. The values were obtained from SINTEF, that did the calculations in WAMIT. The values can be found in Appendix 7.6.

$$\mathbf{A} = \text{diag}\{a_{11} \ a_{22} \ a_{33} \ a_{44} \ a_{55} \ a_{66}\} \quad (3.22)$$

The damping forces are handled by introducing a linear damping term and a non-linear damping term. Documentation of the method of calculation was not available to the author.

$$\mathbf{D} = \mathbf{D}_p + \mathbf{D}_v \quad (3.23)$$

$$\mathbf{D}_p = \text{diag}\{d_{p11} \ d_{p22} \ d_{p33} \ d_{p44} \ d_{p55} \ d_{p66}\} \quad (3.24)$$

Wave Excitation Loads

Wave Excitation loads are found by solving a so called diffraction problem. The body is fixed and only interacting with incident waves. The problem is solved by superimposing the contributions from Froude-Kriloff Loads and diffraction loads.

$$\boldsymbol{\tau}_{wave} = \boldsymbol{\tau}_{FK} + \boldsymbol{\tau}_D \quad (3.25)$$

The Froude-Kriloff loads are found by calculating the pressure on the body from the incident waves, without any disturbance from the body (as if it were not present). The model assumes validity of a long wave approximation.

$$\boldsymbol{\tau}_{FK_i} \approx \bar{a}_{0_i} \rho V \quad i = 1, 2, 3 \quad (3.26)$$

$$\boldsymbol{\tau}_D \approx \bar{a}_{0_i} \mathbf{M}_{A_i} \quad i = 1, 2, 3 \quad (3.27)$$

3.3.4 Control System and Thruster Forces

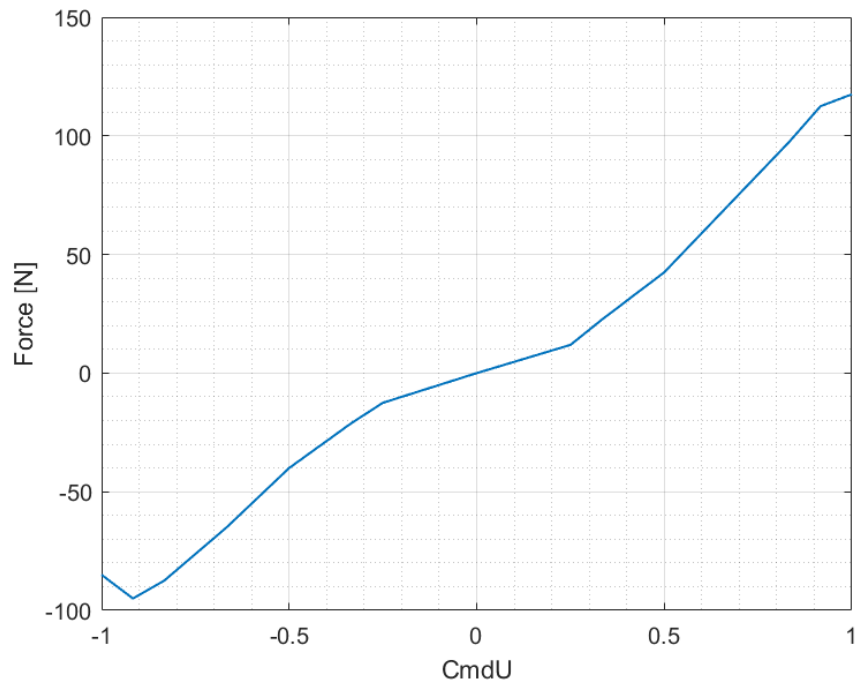


Figure 3.8: Thruster curve

3.3.5 Note on Model Assumptions and Limitations

The ROV force model assumes in general low relative velocities ($u_{rel} < 0.1m/s$). When the body is moving slowly the motion will be less subjected to coupled motions, e.g combined yaw-surge motion when circumnavigating the net. There are however some uncertainty connected with the impact of the pitch-surge coupled motion that can occur in wave lengths of the same order of magnitude as the body.

Numerical Convergence Study on Net Mesh

All numerical models make a compromise between accuracy and computational efficiency. In this section, the discretization error of a given net mesh will be identified to find the best suited mesh resolution of the net.

Other parts of the system are also discretized, such as the floating collar, bridles and anchor lines. However, these parts are assumed sufficiently tested in other studies and do not impact the interaction between the ROV and the net to a significant degree. For these other components the discretization is chosen from expert opinions within SINTEF.

Some similar convergence studies on the net mesh resolution was found in literature. Shen (2018) suggested a mesh resolution of $N_r \times N_v = 24 \times 8$. However, it is worth noting that these tests were conducted under different environmental conditions. In this report, we will expect higher net deformation, since those tests did not include aligned waves in addition to current. Thus the net force model, which is dependent on the relative angle between the net and inflow, is much more sensitive to the mesh resolution under more energetic waves.

The reference parameters for the study are the mean anchor force and the mean drag force on the net. These values give an indication of the motion behaviour of the system. The anchor forces are governed by the motion of the whole fish cage system. Thus a convergence of this value will mean that the translational motion of the center of the cage does not change with higher mesh refinement. Since the anchor forces are averaged over the measuring period, differences in amplitudes of high frequency motions are not considered. The drag forces on the net are important for an accurate description of the net deformations and the wake model. As described in section 3.2.1, the motions of the nodes are governed by the drag forces that act on neighbouring areas of the net. Higher mesh refinements will ensure a more accurate description of the inflow attack angle on the screen.

The strategy applied for the following convergence studies are as follows. Starting at a resolution of $N_r \times N_v = 16 \times 7$, twelve mesh resolutions are tested with an increasing mesh refinement. The number of nodes in the middle of each section are multiplied with the following factors [1 1.5 2 2.5 3 3.5 4], i.e. the nodes at the corner of each section were excluded. This way, the aspect ratio of the elements are kept constant. An example of dividing the mesh into sections can be seen in fig. 4.1

4.1 Current only

A convergence study on a moored fish cage system was performed under the same velocity profile as described in sec. 2.3. The results are shown in fig. 4.2.

The plots do not prove convergence for the highest mesh resolution. Although, the differences in the values are not significant. By plotting the relative difference between a given study and the previous, we can see from fig. 4.3 that the error varies between 0 and 2%. It is worth noting that current velocities in the range of 0-0.35 m/s does

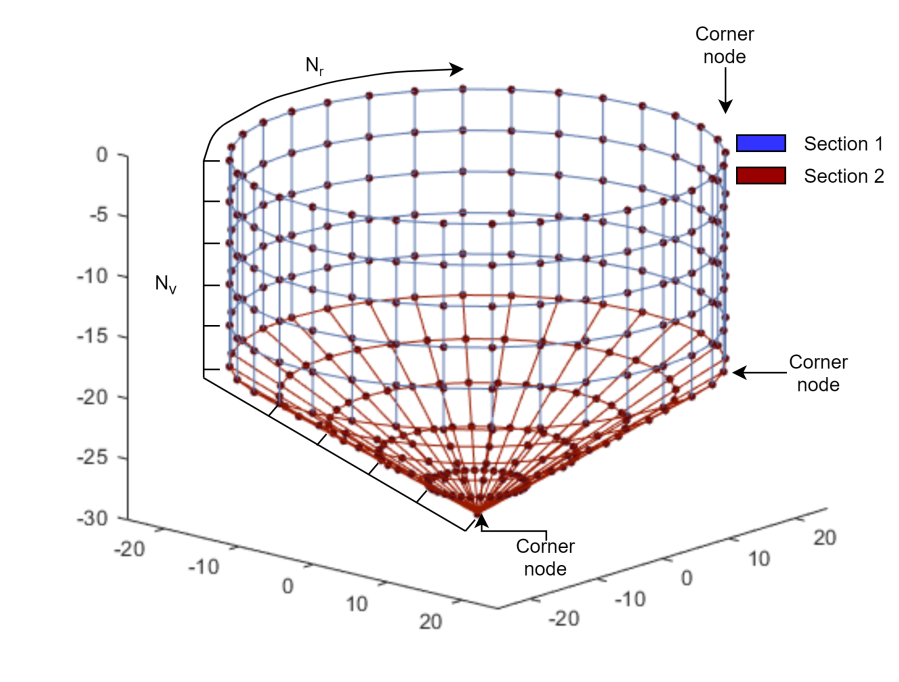


Figure 4.1: Net mesh divided in sections

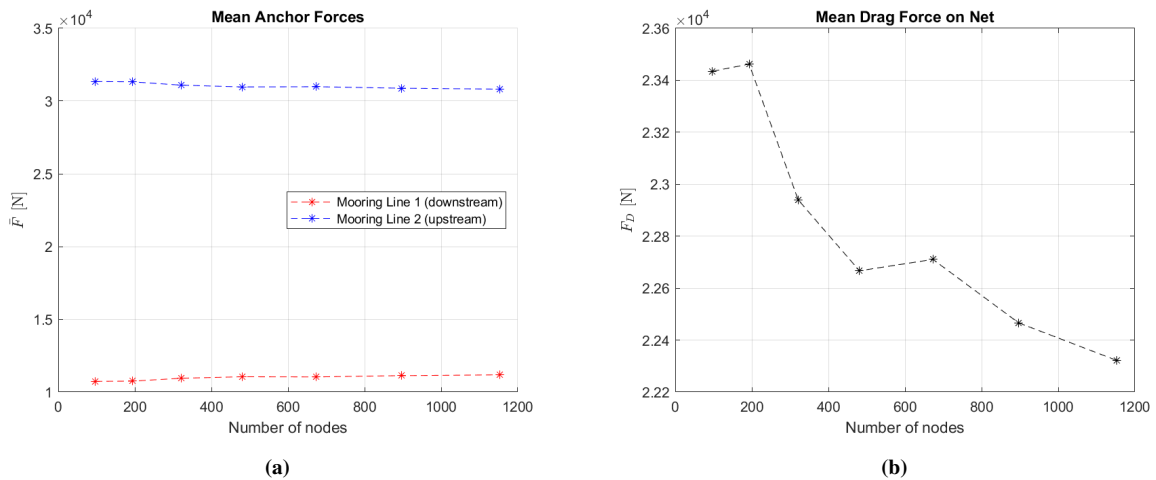


Figure 4.2: Mean anchor forces (a), and mean drag forces (b) with increasing mesh refinement.

not cause large deformations of the net. In general, the requirements for small errors is expected to change with larger velocities.

4.2 Aligned Waves and Current

A convergence study on a moored fish cage system was performed under the same velocity profile as described in sec. 2.3 and using the spectrum for wind generated waves as described in sec. 2.2. The results are shown in fig. 4.4.

We cannot conclude with successful convergence on the largest mesh resolution for aligned was and current either. It is clear that in these conditions the differences are much larger compared to the study with current only. In fig. 4.5, we can see that the improvement of increasing the mesh refinement falls just below 2%.

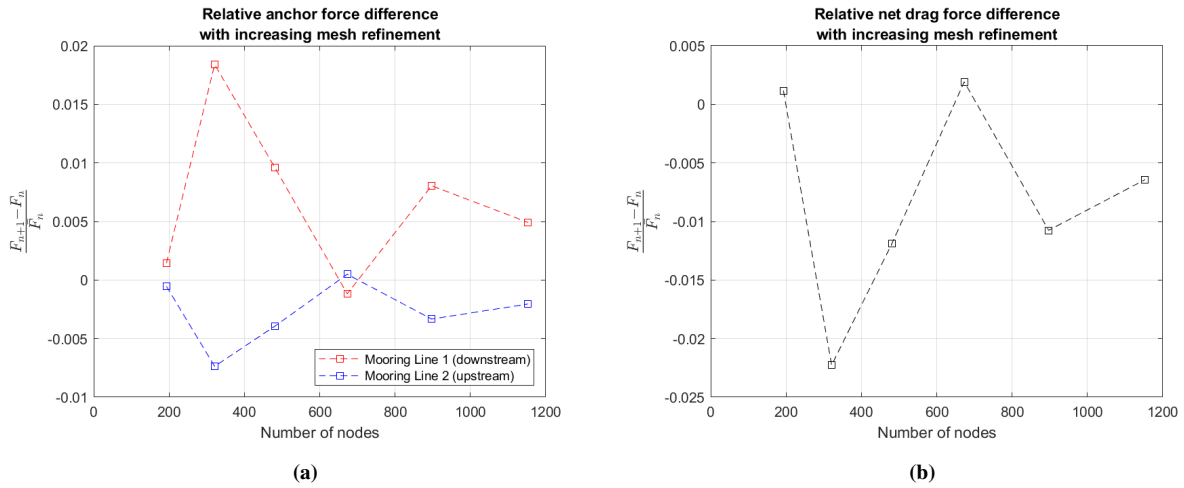


Figure 4.3: Relative anchor forces difference (a), and relative drag forces difference (b) with increasing mesh refinement.

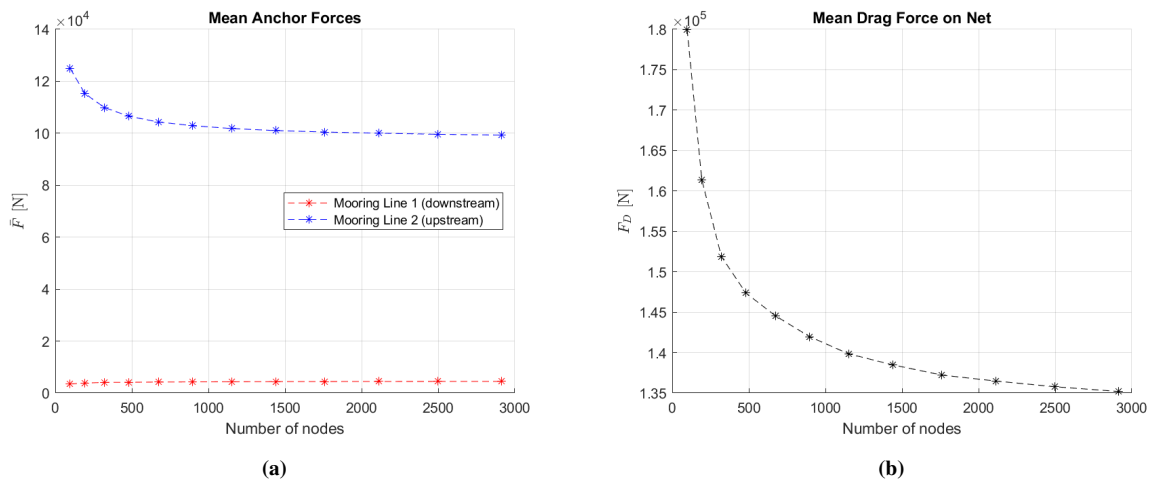


Figure 4.4: Mean anchor forces (a), and mean drag forces (b) with increasing mesh refinement.

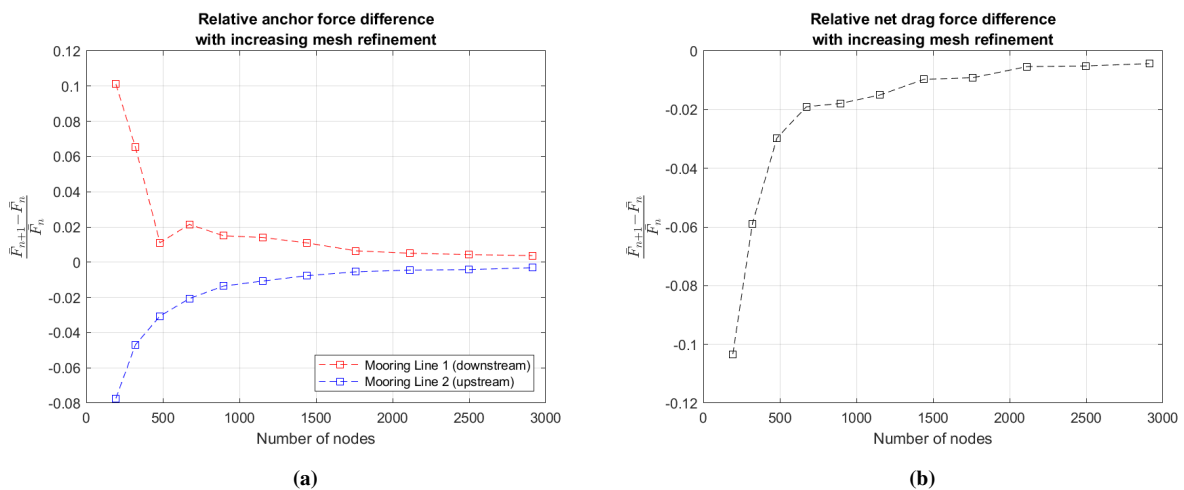


Figure 4.5: Relative anchor forces difference (a), and relative drag forces difference (b) with increasing mesh refinement.

Although simulations of higher mesh refinements are desirable to identify the exact error of each mesh type, this was not done. One of the reasons is that the stability requirements with regards to the time step increased

dramatically. On a Intel Core i7 CPU, larger mesh refinements would take well over 24h (2.4h per minute simulation time), thus a decision was made to use the refinement with 673 nodes, which equals a mesh refinement of $N_r \times N_v = 48 \times 15$. The error compared to the finest mesh of 1153 nodes is 3.4%.

Assesement of net wake effect on ROV

Numerous research have been performed on investigating the characteristics of the wake behind a flat porous panel. There is however no known theory for the velocity deficit of porous cylinders of the fish cage type. In this chapter we will build a mathematical model to calculate the reduced velocity in the flow around a circular fish cage and in the wake. The assumption made is that we can build a solution for a more complex structure based on solutions from screen elements. This is convenient because the structure is already discretized in screen elements from the force model. The model is two-dimensional, meaning that the flow mixing into the wake from underneath the cage is not considered.

5.1 Wake Behind Screens

A screen in this context is defined as a two dimensional porous flat panel. Depending on the solidity ratio, Reynolds number and angle of attack, the screen will experience a drag force obtained from the screen force model (see sec. 3.2.1). For high Reynolds number, a turbulent flow will develop behind the screen. In general, the wake velocity can be described as in eq. 5.21, having a mean velocity component \bar{u} and a fluctuating component u' .

$$u^{wake} = \bar{u} + u' \quad (5.1)$$

In this thesis we will refer to the velocity profile in the wake as the mean velocity component, thus u will be interpreted as \bar{u} . Another important notation in wake equations is the velocity deficit, often denoted u_1 , which is the magnitude that is subtracted from the ambient flow U_∞ .

$$u_1 = U_\infty - u \quad (5.2)$$

According to the momentum theorem, as described by White and Corfield (2006), the drag force associated with the wake profile is independent of the downstream distance x .

$$F_D = \int_{-\infty}^{\infty} \rho \bar{u} u_1 dA = (const) \rho U_\infty u_{1max} b \quad (5.3)$$

This means that the wake profile can be related to the force acting on the body.

5.1.1 Lølands Formula

Løland (1991) showed in his thesis that a good correlation between the wake velocity and drag coefficient of a

screen perpendicular to the inflow could be obtain by a simple equation called *løland's formula*. The method assumes a dependency between the solidity ratio and the wake velocity, thus the drag coefficient is assumed independent of the Reynolds number:

$$u_1 = 0.46C_D(\theta = 0, Sn) \quad (5.4)$$

Here the Reynolds number independent drag coefficient is defines as:

$$C_D(\theta, Sn) = 0.04 + (-0.04 + 0.33Sn + 6.54Sn^2 - 4.88Sn^3) \cos \theta \quad (5.5)$$

The method is proved to be useful as a simple approximation of the velocity reduction compared to the more extensive approach described in sec. 3.2.1. However, method is limited to a range of Reynolds numbers and does not give a complete description of the profile of the wake behind a circular body.

5.1.2 Sum of Cylinders model

The sum of Cylinder model is a method of calculating the velocity deficit behind a body by the use of linearized turbulent wake equations. A section of the net is modelled as a row of solid cylinders as described by Schlichting. The number of cylinders is determined by the mesh size. Assuming a solidity ratio is given, the following relation for the mesh size is given for a square shaped knotless mesh:

$$Sn = \frac{2d}{\lambda} - \left(\frac{d}{\lambda}\right)^2 \quad (5.6)$$

$$\lambda = \frac{2d + \sqrt{(-2d)^2 - 4Sn \cdot d^2}}{2Sn}$$

The mesh size λ is equivalent to the spacing between each cylinder along the screen in our two-dimensional model. The center of each cylinder will act as a source point for an individual velocity deficit profile. A diagram describing the discretization of the cylinders is seen in fig 5.1. The source points of the cylinders are found by making a cross section in the xy-plane, thus only include vertical cylinders. In principle, this approach can be extended to include all the horizontal cylinders as well. Although, including a full 3D-model in the mathematical modelling later does not seem feasible from computational efficiency perspective.

The cylinders are given an equivalent drag force coefficient, such that the sum of the drag force contribution from each cylinder is the same as the total drag force on the screen:

$$F_D^{screen} = \sum_{i=1}^N F_{D_i}^{cylinder} \quad (5.7)$$

$$C_{D_i} = \frac{C_D^{screen} \cdot A}{\sum_{i=1}^N d_i l_i}$$

$$C_{D_i} = \frac{C_D^{screen}}{Sn}$$

The solution for the velocity deficit on a single cylinder is given by Schlichting:

$$u_1^{cylinder} = \frac{1}{4\pi} C_D U_\infty \sqrt{\frac{\pi U_\infty}{\epsilon_\tau x}} \exp\left(-\frac{y^2 \cdot U_\infty}{4\epsilon_\tau x}\right) \quad (5.8)$$

The virtual kinematic viscosity ϵ_τ is given by semi-empirical formula, derived from measurements by Schlichting:

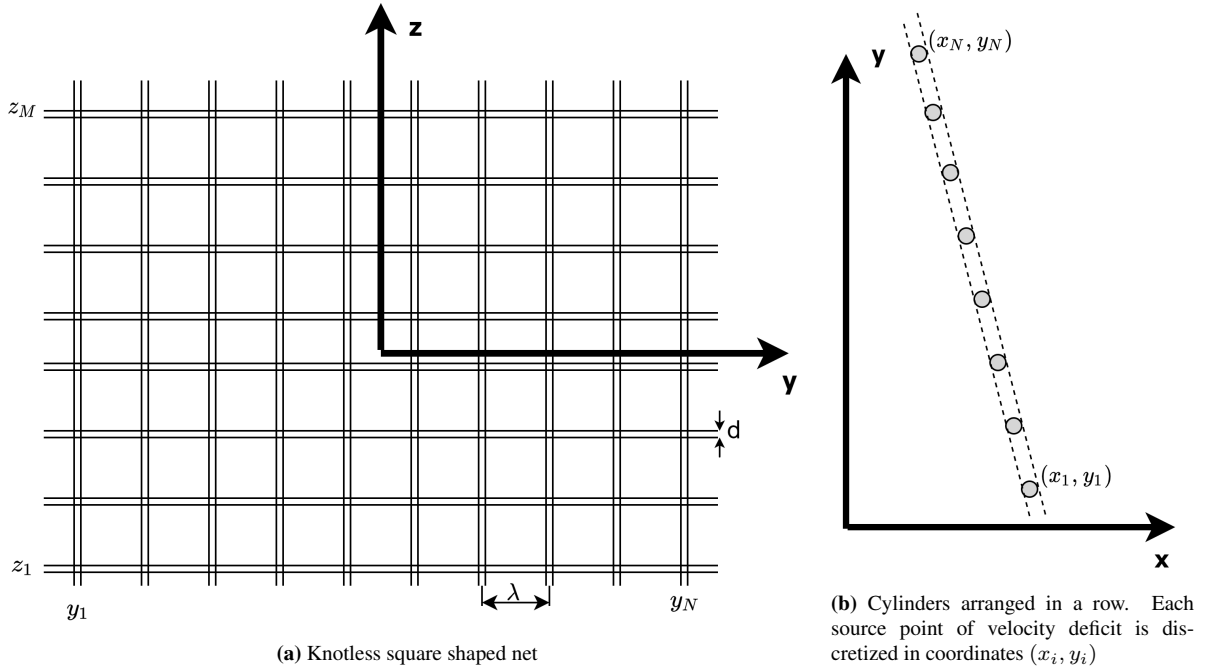


Figure 5.1: Diagram describing the components of the "sum of cylinder model"

$$\epsilon_\tau = 0.0222U_\infty C_D \cdot D \tag{5.9}$$

The velocity deficit behind the screen will be calculated by superimposing the velocity deficit from each cylinder:

$$u_1 = 0.95U_\infty \sum_{i=1}^N \sqrt{\frac{C_{D_i} \cdot d_{tw}}{(x - x_i)}} \exp\left(-\frac{(y - y_i)^2}{0.0888C_{D_i} \cdot d_{tw}(x - x_i)}\right) \tag{5.10}$$

Here the interpretation of the ambient velocity U_∞ is the inflow velocity on the screen. The

In the case of several consecutive screens, the velocity profile of the wake will therefore converge towards the velocity in front of that screen. This will cause a discontinuity at the boundary of wake profile. An example of the wake behind a single screen is shown in fig 5.2a and the wake behind two screens in tandem configuration. We will solve this by introducing an plane turbulent mixing equation that distributes the velocities on both sides of the discontinuity symmetrically.

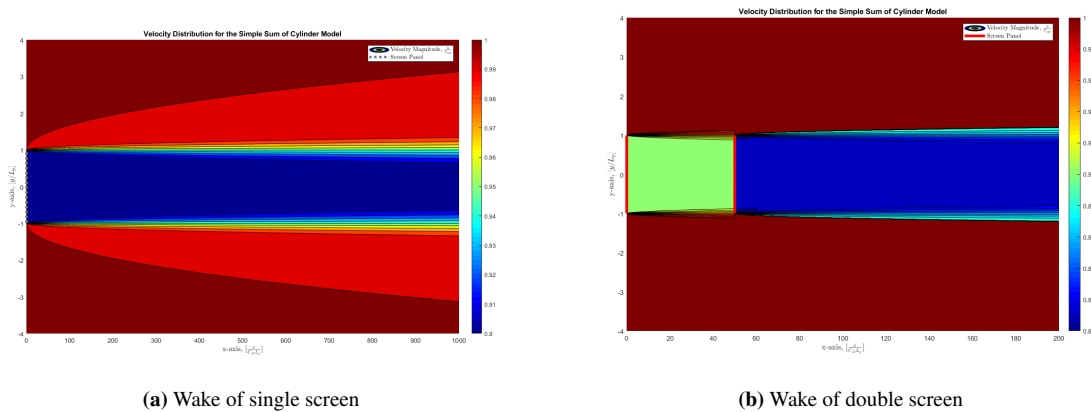


Figure 5.2: Velocity contours of the reduced velocity for two screen configurations. $Re^{cyl} = 3085, C_D = 0.4, C_{D_i} = 1.2$

5.1.3 Plane turbulent mixing

The fluid flow exiting the screen and the outside free flow is separated. Due to shear stress between the two layers, it is expected that the two layers will mix from the point of separation. Görtler (1942) proposed a solution for the mixing layer between to laminar flow regions by assuming a profile anti-symmetrical about the midpoint:

$$u(x, y) = U_1 + \frac{U_2 - U_1}{2} \left[1 + \operatorname{erf} \frac{\sigma y}{x} \right] \quad (5.11)$$

,where $\operatorname{erf} z$ is the error function defined by eq. 5.12 and is defined on the interval $[-1, 1]$. The error function essentially scales the mean value between the two separated flows over a varying width $b(x)$ downstream.

$$\operatorname{erf} z = \frac{1}{\sqrt{\pi}} \int_0^z e^{-(z')^2} dz \quad (5.12)$$

A schematic representation of the mixing layer is shown in fig 5.3.

As Görtler (1942) suggested, the parameter σ is found empirically. He found that $\sigma = 13.5$ fitted an experiment where $U_1/U_2 = 0.5$. The angle α can be used as a reference to experiments and is found by solving the following expression:

$$\alpha = \tan^{-1} \left(\frac{b(x)}{x} \right) = \left(\tan^{-1} \frac{1}{\sigma} \left(\operatorname{erf}^{-1} \left(\frac{0.02U_2}{U_2 - U_1} \right) \right) \right) \quad (5.13)$$

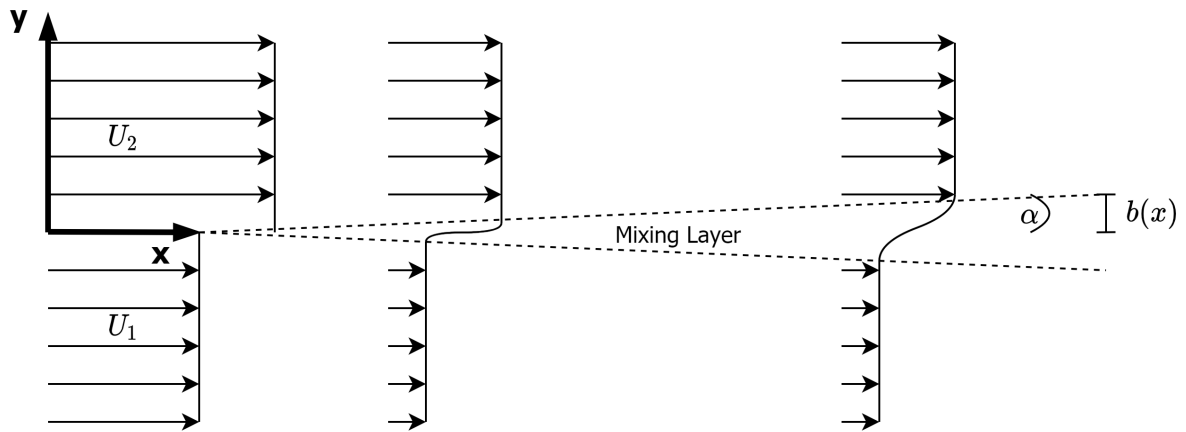


Figure 5.3: Diagram of plane mixing layer between two separated flows

5.2 Flow through and around cage

A circular fish farm exposed to current in a sea environment will often result in a turbulent flow field inside the cage and in the wake. In our model we will assume that the flow in front of the cage and outside the wake is inviscid. The flow in the wake is modelled as a mean velocity deficit from the potential flow. The velocity deficit is determined from a 2D plane wake model. The two flow regions are shown in fig 5.4

5.2.1 Wake Model Methodology

The mathematical model of flow through and around a porous cylinder will be presented in the following subsection. The procedure can be summarized in the following steps.

1. Calculation of potential flow velocities outside wake

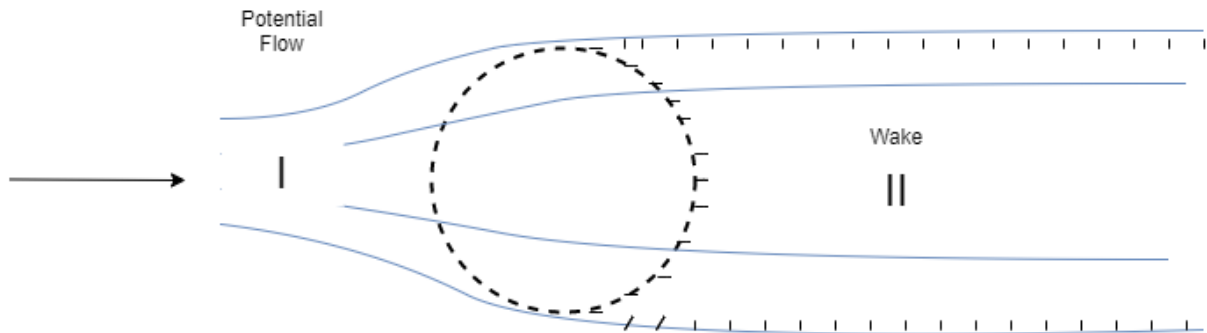


Figure 5.4: Schematic of cylinder cross flow. Flow region I is modelled as inviscid, flow region II is modelled as plane wake

2. Calculation of mean velocity deficit in wake by sum of cylinder model
3. Connecting the wake and potential flow with plane turbulent mixing as formulated by Görtler (1942)

A program is created in MATLAB for development and testing purposes of the method on a static 2D net cage. Later the methodology is adapted to be written in to the source code of the FhSim software. A flow chart of the MATLAB program as well as the code is given in appendix 7.7. In the MATLAB program a discretization of the flow field and net is made, as well as drag force calculations prior to the wake model.

The FhSim code, written in C++ language, was implemented as a subroutine inside the object that calculates everything associated with the ROV. The structure of this code differs from the MATLAB version in the way that only one point in space needs to be calculated each time step. Also, drag coefficients and element discretization from the net model of the program was used to perform the calculations. Due to confidentiality restrictions, the program cannot be published, but a flow chart of the code is shown in fig 5.5.

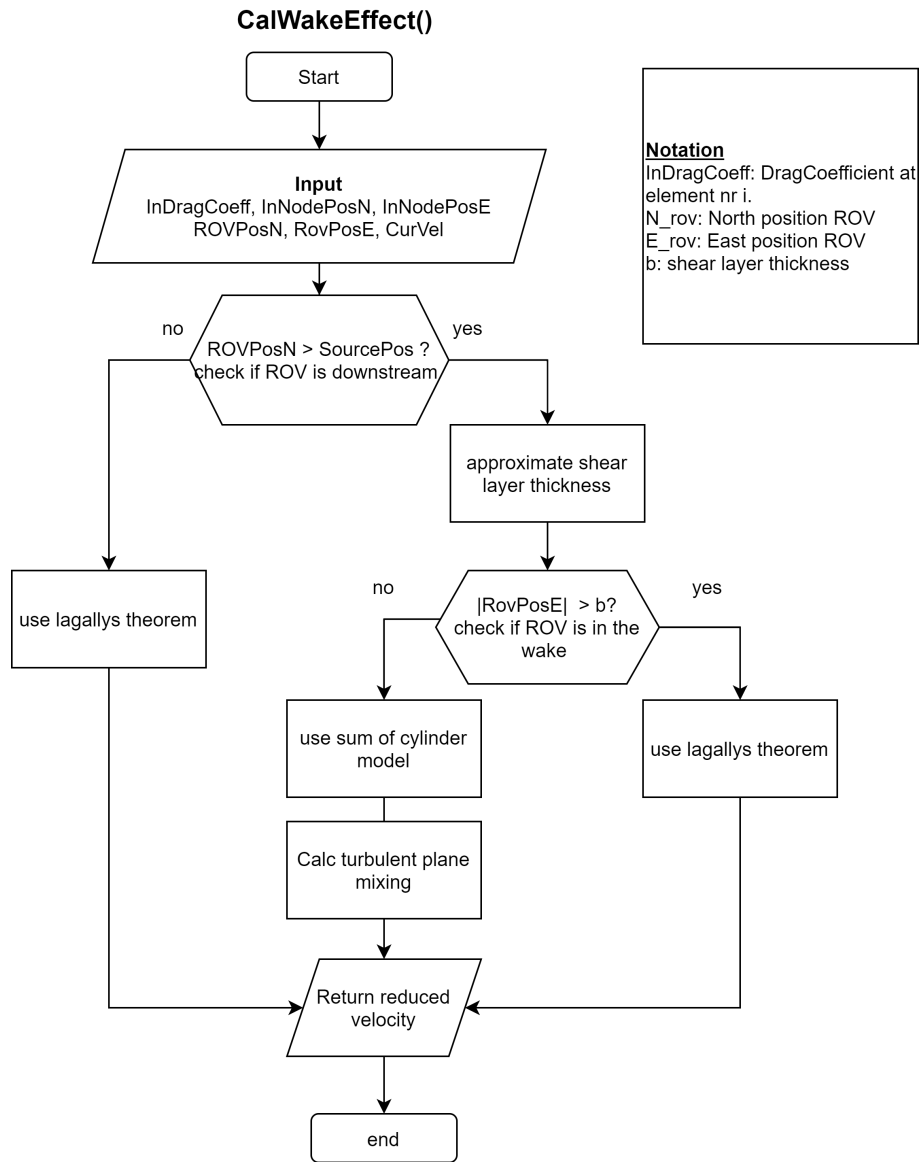


Figure 5.5: FhSim Wake Model Flow Chart

Potential Flow

We will assume that the flow in region I can be modelled as a potential flow generated by a source of equivalent resistance as the body. From the screen model approach of calculating drag forces on segments of the cylinder, we already know the total drag coefficient on the cylinder given by eq. 5.14.

$$C_D = \frac{F_D}{\frac{1}{2}\rho U_\infty^2 D} \quad (5.14)$$

where F_D is the total drag force on the body given as a summation of the drag force on the individual screen elements.

$$F_D = \sum_{i=1}^N \frac{1}{2}\rho C_{D_i} U_i^2 L_i \quad (5.15)$$

, where subscript i denotes the element number, L_i the length of each element and U_i is the incoming velocity at each element.

We will place a "log-r" source in the centre of the cylinder (origin) which will create a dividing streamline that resembles the streamline patten seen from experiments conducted by Gansel et al. (2008). The source strength \mathbf{q} will be determined from Lagally's theorem (5.16).

$$\mathbf{q} = \frac{1}{2}C_D D U \quad (5.16)$$

We will solve the velocity potential in the whole calculation domain to begin with. The resulting potential is given by superimposing the free flow potential Φ_0 and the source potential Φ_{source} as in eq. 5.17.

$$\Phi = \Phi_0 + \Phi_{source} = Ux + \frac{\mathbf{q}}{2\pi} \log \sqrt{x^2 + y^2} \quad (5.17)$$

The streamfunction is defined as in eq 5.18.

$$\Psi = \Psi_{source} = \frac{q}{2\pi} \theta \quad (5.18)$$

The velocity components are given as derivatives of the potential.

$$u(x, y) = \frac{\partial \Phi}{\partial x} = U + \frac{\mathbf{q}}{2\pi} \frac{x}{x^2 + y^2} \quad (5.19)$$

$$v(x, y) = \frac{\partial \Phi}{\partial y} = \frac{\mathbf{q}}{2\pi} \frac{y}{x^2 + y^2} \quad (5.20)$$

An example of the solution to the potential flow is shown below.

Wake

The wake is the disturbed flow behind a body caused by turbulence. For a porous cylinder the turbulence will be caused by the flow separation at the flanks and the cross flow over the individual twines in the net. Separation occur close to the cylinder in the region $\pi/4 < \theta < \pi/2$, as for a solid cylinder. Different from a the solid cylinder is that flow is moving through the net. The cross flow can be typically characterized with a Reynolds's number $\mathcal{O}(10^7)$, which cause a turbulent wake behind each individual twine.

The wake flow is not stationary and can generally be described by a mean component and a fluctuating component. We will model the velocity deficit of the mean flow based on a 2D plane wake model.

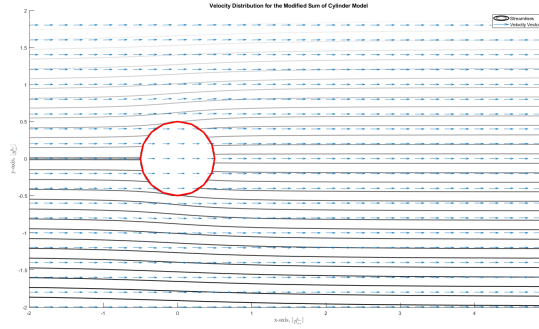


Figure 5.6: [Stream lines and velocity vector plot of cylinder cross flow

$$u = \bar{u} + u' \quad (5.21)$$

The velocity deficit \bar{u}_1 in the wake will be defined relative to the potential flow. This is because the source is inducing a positive horizontal velocity downstream of the body. This potential flow in the wake is artificial, but will be corrected for as the increased velocity in the wake will be used as input velocity for the wake flow equation.

$$u_{wake} = u_{potential} - \bar{u}_1 \quad (5.22)$$

The 2D wake flow equation, derived by (Løland, 1991, p.29-30), is based on a Fourier transformation of an initial condition at $x=0$. He argues that $u_1(x=0, y) = aU_\infty$ for $-L/2 < y < L/2$ where $a = \frac{1}{2}C_D$. The factor a is related to the reduction factor $r = 1 - a$. The resulting equation is shown below.

$$u_1(x, y) = \frac{1}{2\pi} a U_\infty 2 \left[\frac{\pi}{2} \left[\operatorname{erf} \left(\frac{D/2 + y}{2\sqrt{\epsilon x/U_\infty}} \right) + \operatorname{erf} \left(\frac{D/2 - y}{2\sqrt{\epsilon x/U_\infty}} \right) \right] \right] \quad (5.23)$$

, where ϵ is the virtual kinematic viscosity, $\operatorname{erf}(z) = \frac{2}{\sqrt{\pi}} \int_0^z e^{-z'^2} dz'$ is the error function. Given $a = \frac{1}{2}C_D$, the asymptotic expansion Taylor expansion of eq. 5.23 ($x \gg \delta_1$) is as follows.

$$u_1(x, y) = \frac{C_D \cdot D}{4} D \sqrt{\frac{U_\infty}{\epsilon x \pi}} \exp\left(-\frac{y^2 U_\infty}{4\epsilon x}\right) \quad (5.24)$$

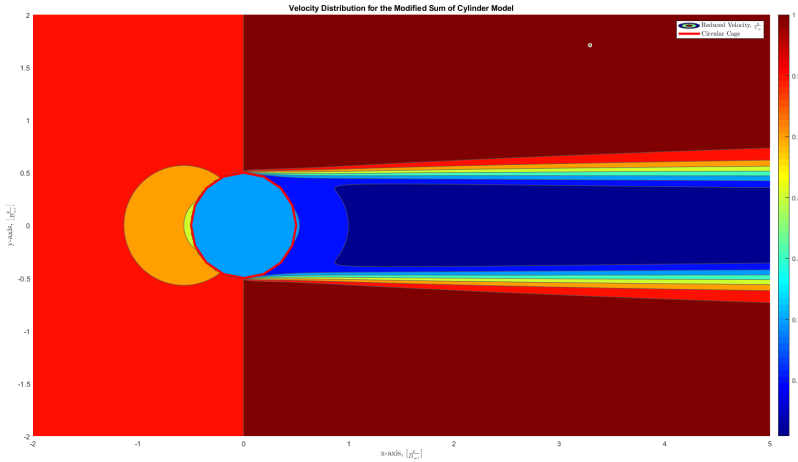
This implies that the velocity decay of $u_1(x, y)$ is proportional with \sqrt{x} , which is in correlation with the power laws for jets and wakes stated in (White and Corfield, 2006, p. 485). The function has its origin at the center of the cylinder, which implies that the model is probably inaccurate in close proximity to the net.

The main uncertainties connected with the model is the value of a and ϵ . Experiments conducted by Løland (1991) proves that the reduction factor of $r = 1 - 0.46c_D$ behind a flat panel is a good assumption, which will imply that $a = 0.46c_D$.

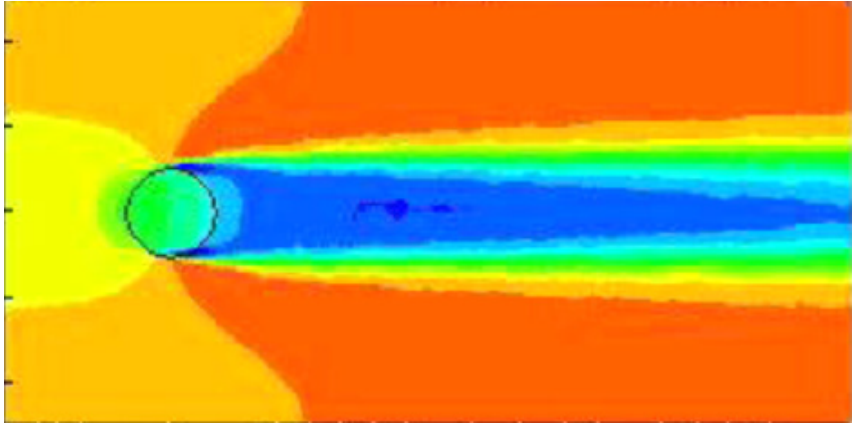
The virtual kinematic viscosity ϵ is taken as an empirical value given by Schlichting and takes the form.

$$\epsilon = 0.0222 C_D D U_\infty \quad (5.25)$$

An example of flow is shown in fig 5.7a by a contour plot of horizontal velocity components.



(a) Example of wake model calculations



(b) CFD calculations by Zhao et al. (2013)

Figure 5.7: Contour plots of horizontal velocity components. Note that the scaling of the color codes are different.

5.2.2 Wake Model Comparison With Experiments

The mathematical model has been compared with experimental result obtained by Gansel et al. (2008) as can be seen in fig 5.8. The study measured the velocity at 3 different distances downstream in the wake by use of PIV instruments. As can be seen when comparing the markers and the solid lines, the model overestimates the velocity deficit close to the cage and underestimates the decay of the velocity deficit to a small degree. In the experiment there is an acceleration of the flow at the flanks which is remains further out from the wake. However, overall there is a good correlation between experimental data and the model. Notably, Løland's formula is a reasonable approximation in the center of the wake. No experiments could be found to validate the flow upstream of the cage.

This experiment has similar twine diameter to what is being used in the simulations, thus the Reynolds number of the flow over each twine is similar as a full scale experiment. It is also suggested by the authors of the experiment that the turbulence of the wake is mainly created by the flow over each twine. Therefore this scaled model resembles the same properties as we will use in the simulations.

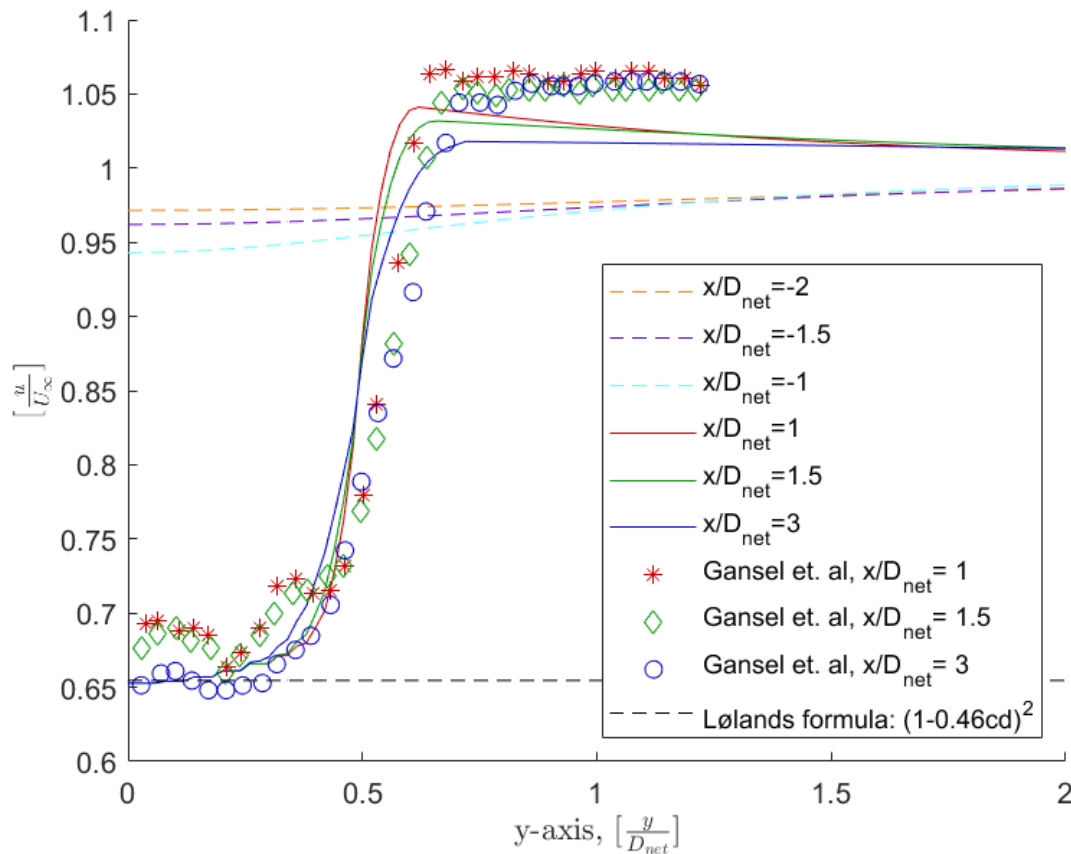


Figure 5.8: Comparison between wake model and experimental data. Scattered points represent experimental data from Gansel et al. (2008), lines represent wake model.

Something that is not addressed in the experiment by Gansel et al. (2008) is the effect of the Reynolds number of the flow over the cylinder diameter. Since a full scale model typically is 50 times larger than this experiment, it is unclear whether this changes the size of the shear layer. In this report we will assume that the growth rate of the shear layer increases proportionally to the diameter. Thus, the shape of the net will remain the same independent of the diameter of the net.

Time Domain Simulations of ROV Trajectory

The time domain simulation setup is created to capture most of the challenges a ROV will face when navigating around a typical fish cage. The different scenarios are named "Mission 1-4", and represent a situations for the ROV where the environmental loads are affecting the interaction between the ROV and the net differently.

A schematic of all the missions are shown in 6.1. During mission 1-3, the ROV is placed at a position 2m below the free surface for 100 s. This allows the ROV to adjust to the target distance to the net of 2.5 m. Also, the fish cage will withing 100 s reach a steady state of oscillation with regards to the surge motion of the system. This is important, because the net will during the transient state (0-100s) undergo large motions that is nonphysical in a real aquaculture locations.

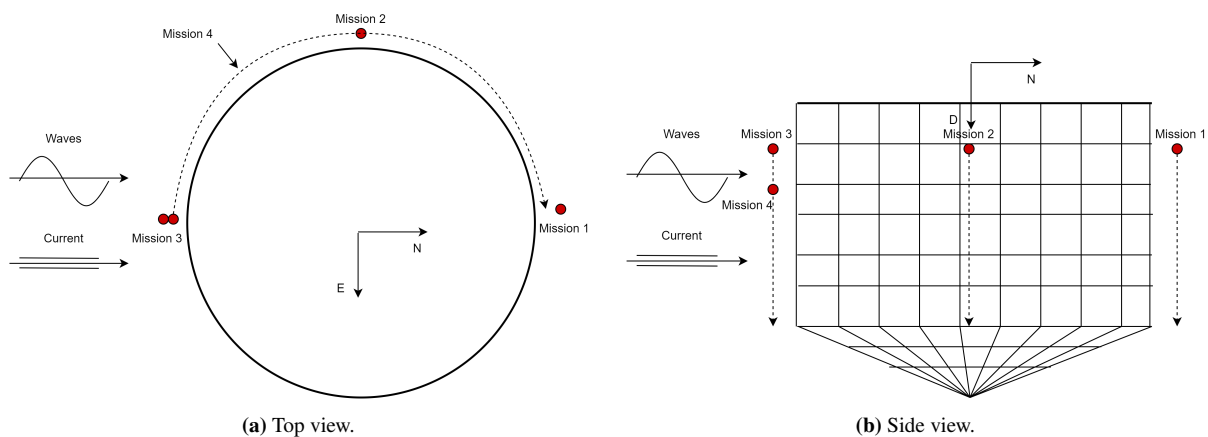


Figure 6.1: Schematic of setup for the simulated missions. Mission 1-3 are descending vertically along the net. Mission 4 is circumnavigating the net at a fixed depth. Axis shown is an earth-fixed North-East-Down coordinate system.

After the 100 initial seconds, the ROV in mission 1-3 is set a fixed vertical speed such that it follows the net at the target distance of 2.5 m. It is important to notice that the actual vertical speed of the ROV is dependent on how much thruster force the ROV has to use in order to stay upright and close to the target distance to the net, due to the environmental loads from waves and current.

For mission 4, the ROV is positioned at a depth level of 5m, which the control system is targeting to keep. Also, for this mission the target is to keep the ROV at 2.5 m from the net. At initiation, the ROV will circumnavigate the fish cage at a set circumferential velocity. Although, as for the previous navigation missions, the actual velocity is dependent on the motion of the net and the environmental loads affecting the ROV.

Table 6.1: Initial position parameters

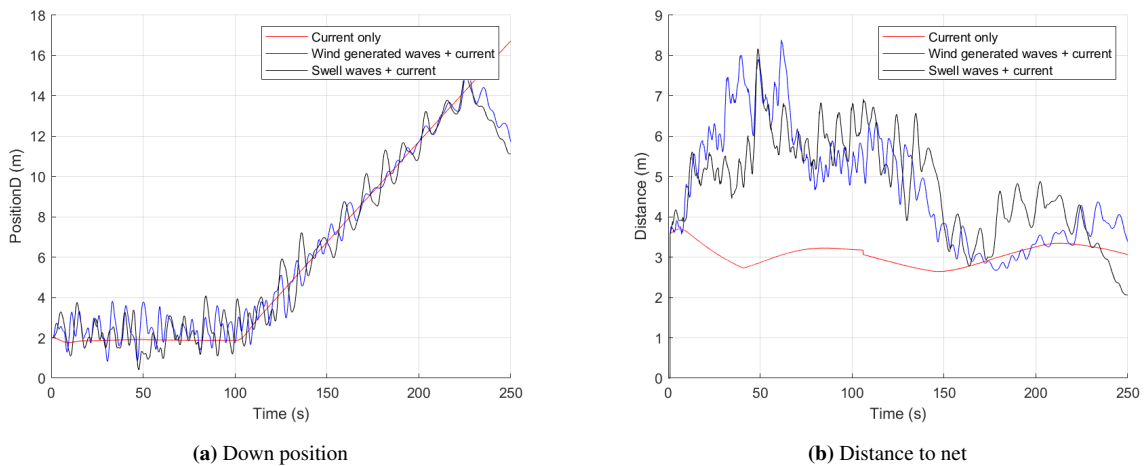
	Mission 1	Mission 2	Mission 3	Mission 4
N_0 [m]	28.5	0.0	-27.5	40.2
E_0 [m]	0.0	-27.5	0.0	11
D_0 [m]	2.0	2.0	2.0	5.0
Dist [m]	2.5	2.5	2.5	2.5

6.1 ROV Response Around a Rigid Net

In order to investigate the effect the environmental loads has on the performance of the ROV in sea conditions, we will first isolate the problem to only include the ROV. The ROV will be guided along a rigid net structure, i.e no net motion are present. In that way, the target distance to the net will not be impacted by the motion of the net it self.

Key results from the simulation follows in fig. 6.2, 6.8 and 6.9. Here we investigate the ROVs position during the mission and the distance to the net, with respect to time. Since the net is kept fixed, the motion of the ROV is only affected by hydrodynamic forces acting on the body.

6.1.1 Mission Number 1

**Figure 6.2:** Results from mission number 1 around a rigid net

When the ROV is descending at the downstream section of the net we observe that the waves causes oscillations in the vertical position D . Generally there is a tendency for the swell waves to cause larger amplitudes. This is due to the longer wave components that randomly occur. Looking at the distance to the net, we observe that there are oscillations also for the "current only" case. This tells us that when the control system is fixed on a point and subjected to a constant pressure force, the inertia of the ROV will cause a latency on the predicted necessary force.

6.1.2 Mission Number 2

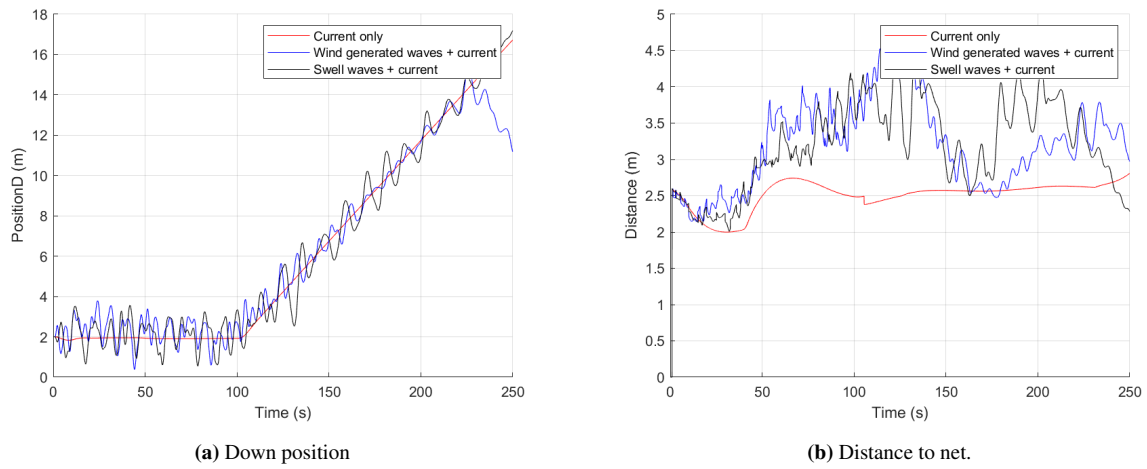


Figure 6.3: Results from mission number 2 around a rigid net

For mission number 2 we observe a similar tendency as mission number 1. Here the waves and currents are hitting the ROV on the starboard side, but this gives no significant difference in the vertical oscillations. Notably the amplitudes of the distance to the net are smaller.

6.1.3 Mission Number 3

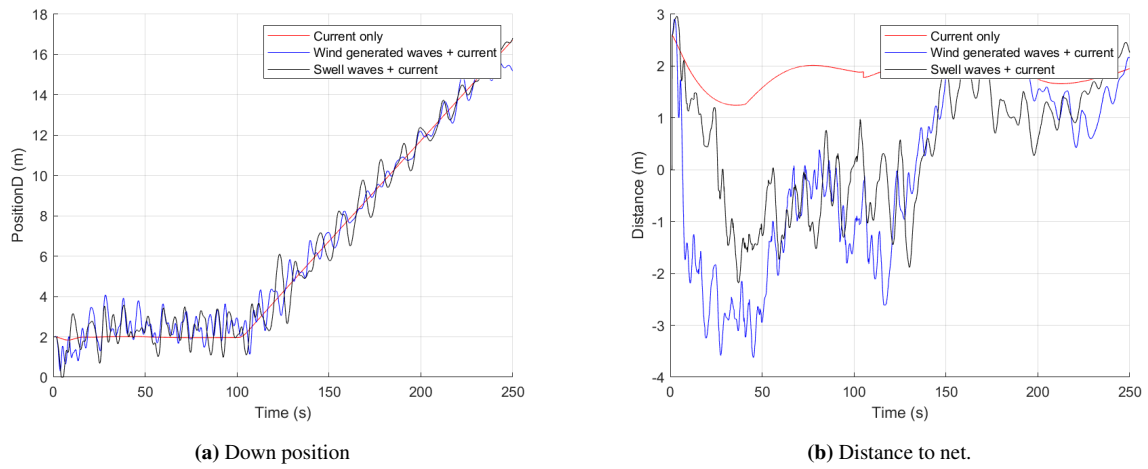


Figure 6.4: Results from mission number 3 around a rigid net

6.1.4 ROV Response Sensitivity to Sea Condition

The results from simulations without fish cage present in fig. 6.2, 6.8 and 6.9 show in general that waves have large influence in the ROV's ability to navigate on a straight path. For the vertical position D, and the distance to the net we can observe oscillations for the simulations including waves. The simulations only including current follow almost straight path on the way down.

Prior to the study, some uncertainty was connected to how far down the wave forces had an impact on the motion of the ROV. Looking at the vertical position D of all missions, oscillations are present at all depths down to 15 m. The amplitude of the oscillations seems to decay slightly on the way down, although the response is also a subject to random incoming waves due to the irregular sea.

A general remark on the simulations with waves are that the motions are sometimes very large, when certain waves are incoming. It will seem like the control system is unable to react sufficiently to longer waves. That is based upon how the motion in swell waves, that consists of longer waves, yields larger motions.

6.2 ROV Response Around a Moored Fish Cage

6.2.1 Mission Number 1

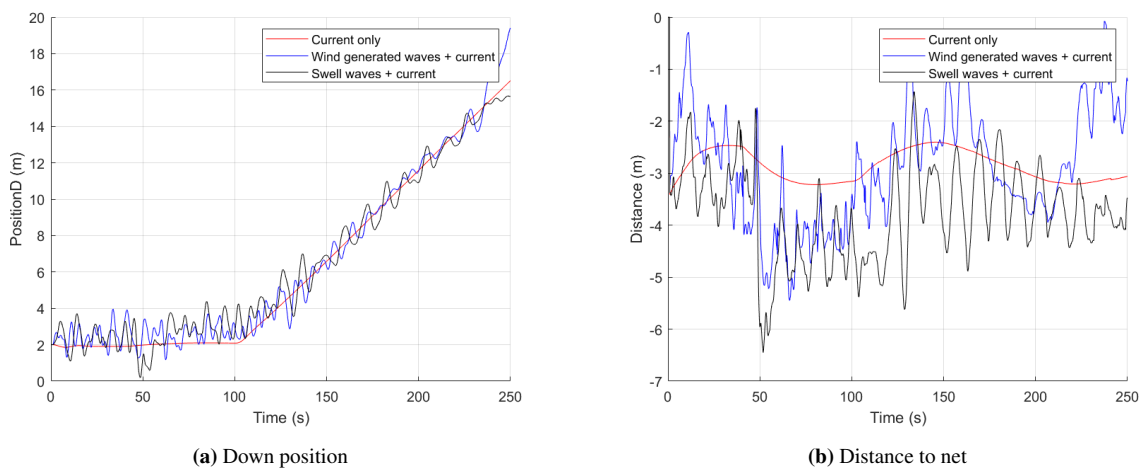


Figure 6.5: Results from mission number 1 with fish cage.

6.2.2 Mission Number 2

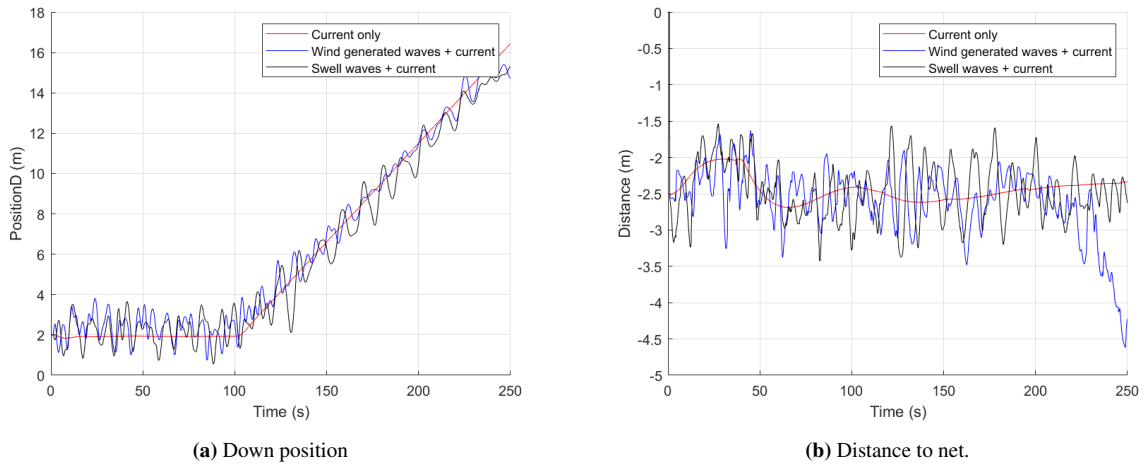


Figure 6.6: Results from mission number 2 with fish cage.

6.2.3 Mission Number 3

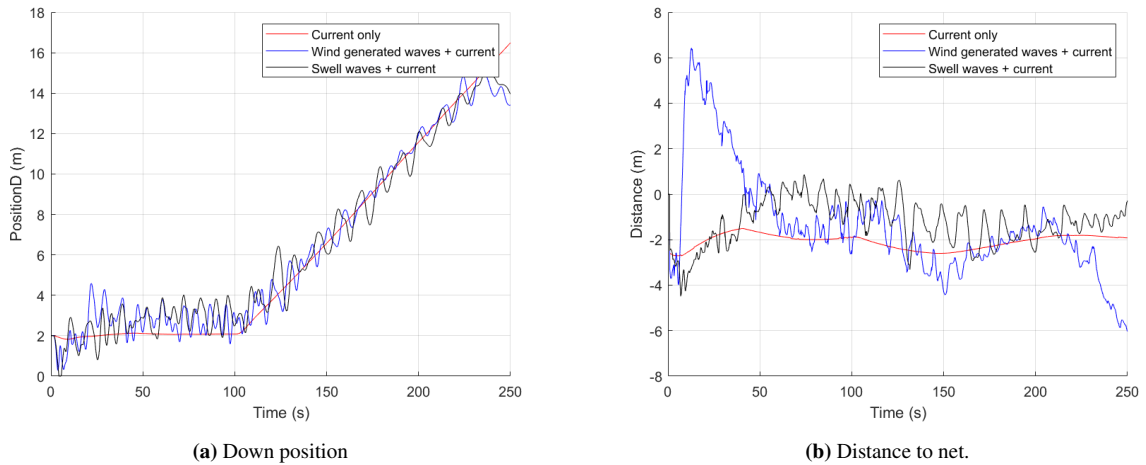


Figure 6.7: Results from mission number 3 with fish cage.

6.2.4 Mission Number 4

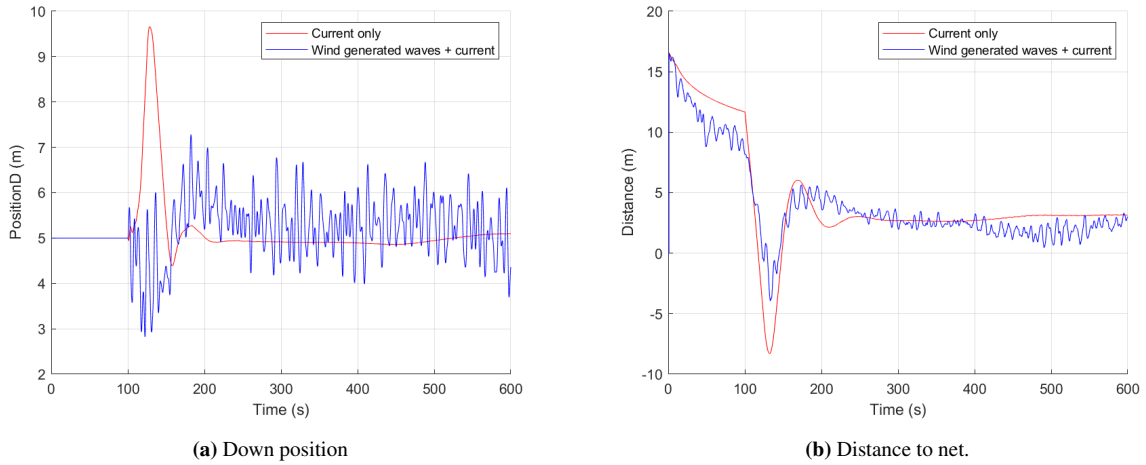


Figure 6.8: Results from mission number 4 with fish cage.

6.3 ROV Response Around a Moored Fish Cage Including the Wake Model

6.3.1 Mission Number 4

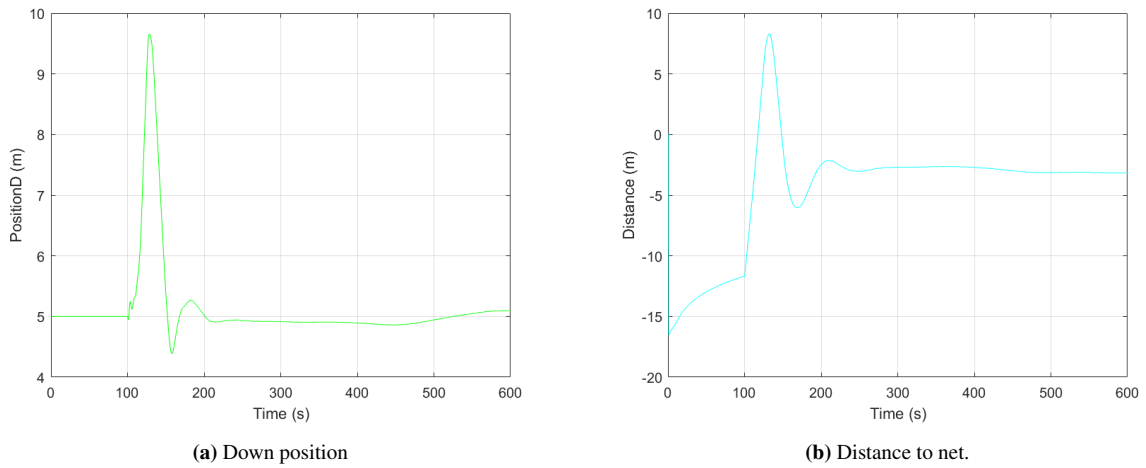


Figure 6.9: Results from mission number 4 with fish cage and wake model.

Conclusion

7.1 Environmental Loads

Weather data from a buoy at Tristeinen was analyzed obtain reference for establishment of a sea condition model for use in simulations. The target was to create conditions that represent waves and currents under the operational limit of an ROV mission. It was found that two different wave spectrum could be defined by; a swell dominated sea state and a wind dominated sea state. The model used for creating the spectra was the simplified Torsethaugen spectrum. Components of 100 regular waves was calculated from the spectrum as input to the program.

From the current data a velocity profile was chosen from the same 1-hour sea state as the wind dominated sea. Although a thorough investigation of validity of common assumptions on current modelling was conducted. For low mean current velocities (e.g 0-0.2 m/s), the assumption of a uniform flow direction is invalid according to this data set. For higher velocities the hourly change in velocity direction was mainly distributed between -25 and 25 deg, with the highest probability density around 0 deg. The standard deviation of the current direction in each depth layer was also significantly small for $\bar{U} > 0.2$ m/s that uniform flow direction is a reasonable assumption.

The result should not be interpreted as a generalization of wave and current behaviour at aquaculture locations, but rather as a reference to how wave and current models can be established.

7.2 Wake Model

A method of calculating the mean velocity deficit in the wake behind a fish cage was developed inspired from the work of Løland (1991). Linearized turbulent wake equations from cylinders that resembles the twines of a net was utilized to calculate the wake flow. Connection with the inviscid flow outside of the wake was done by theory on turbulent plane mixing by Görtler (1942).

The flow outside of the wake was found by implementing a potential source in the center of the cage, where the strength is found from Lagally's theorem. The model showed a similar shape of the velocity profile compared with an experiment conducted by Gansel et al. (2008). The experiment used similar twine diameter as in the net model obtain from SINTEF, thus the turbulence caused by the net is also similar.

7.3 Time Domain Simulations

Simulations for 4 different "missions" was carried out; 3 descending missions at three different positions and 1 circumnavigating. The results have shown that the assumed operational limit of $H_s=1.6$ might have been to high

for the ROV modelled and the control system to react to large waves.

7.4 Recommendations for further work

Some uncertainty remains regarding the impact of the net diameter on the growth of the width of the wake, as no studies were found that measures the wake velocity in full scale experiment.

An important part of the cage that was not analyzed in this thesis is the flow inside the cage. Here we only assume validity of Løland's formula for calculation of inflow on downstream panels. Some experimental data will provide usefully as a benchmark to see if this assumption is valid for all regions inside the cage.

Lastly as a suggestion for further work a statistical study of several time realization of the waves should be conducted. In this thesis the phase angle of the wave has been kept constant for all simulations.

Bibliography

- Argus, 2020. Argus remote system as. URL: <https://www.argus-rs.no>. accessed on: 02.10.20.
- Blevins, R., 2003. Applied fluid dynamics handbook. malabar, fla.
- Enerhaug, B., Føre, M., Endresen, P.C., Madsen, N., Hansen, K., 2012. Current loads on net panels with rhombic meshes, in: ASME 2012 31st International Conference on Ocean, Offshore and Arctic Engineering, American Society of Mechanical Engineers Digital Collection. pp. 49–60.
- Faltinsen, O., 1993. Sea loads on ships and offshore structures. volume 1. Cambridge university press.
- Fossen, T.I., 2011. Handbook of marine craft hydrodynamics and motion control. John Wiley & Sons.
- Gansel, L.C., McClimans, T.A., Myrhaug, D., 2008. The effects of fish cages on ambient currents, in: ASME 2008 27th International Conference on Offshore Mechanics and Arctic Engineering, American Society of Mechanical Engineers Digital Collection. pp. 537–543.
- Goldstein, S., 1965. Note on the condition at the surface of contact of a fluid with a solid body. Modern Development in Fluid Mechanics 2.
- Görtler, v.H., 1942. Berechnung von aufgaben der freien turbulenz auf grund eines neuen näherungsansatzes. ZAMM-Journal of Applied Mathematics and Mechanics/Zeitschrift für Angewandte Mathematik und Mechanik 22, 244–254.
- Kristiansen, T., Faltinsen, O.M., 2012. Modelling of current loads on aquaculture net cages. Journal of Fluids and Structures 34, 218–235.
- Lader, P., Kristiansen, D., Alver, M., Bjelland, H.V., Myrhaug, D., 2017. Classification of aquaculture locations in norway with respect to wind wave exposure, in: ASME 2017 36th International Conference on Ocean, Offshore and Arctic Engineering, American Society of Mechanical Engineers Digital Collection.
- Løland, G., 1991. Current forces on and flow through fish farms (ph. d. thesis). University of Trondheim .
- NS9415, N.S., 2009. E: 2009-marine fish farms-requirements for site survey, risk analyses, design, dimensioning, production, installation and operation. Standards Norway, Norway .
- Schlichting, H., . 1979, boundary-layer theory.
- Shen, Y., 2018. Operational limits for floating-collar fish farms in waves and current, without and with well-boat presence .

- Torsethaugen, K., Haver, S., et al., 2004. Simplified double peak spectral model for ocean waves, in: The Fourteenth International Offshore and Polar Engineering Conference, International Society of Offshore and Polar Engineers.
- White, F.M., Corfield, I., 2006. Viscous fluid flow. volume 3. McGraw-Hill New York.
- Zhao, Y.P., Bi, C.W., Dong, G.H., Gui, F.K., Cui, Y., Xu, T.J., 2013. Numerical simulation of the flow field inside and around gravity cages. *Aquacultural engineering* 52, 1–13.

Appendix

7.5 Net Mesh Creator in MALAB

(See digital file netmesh.m)

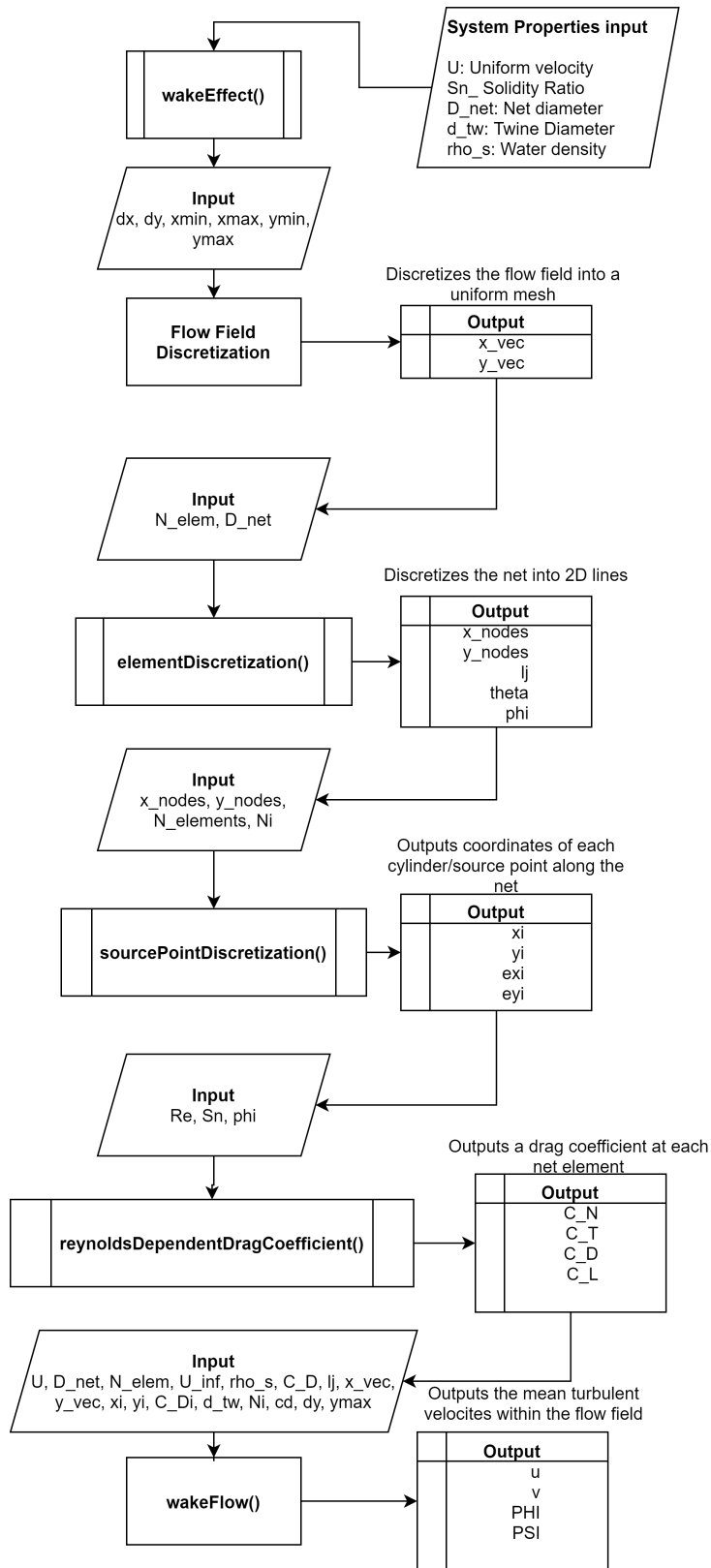
7.6 ROV Properties and Parameters

The following table lists every relevant parameter used in the calculation of the ROV model. The implementation of these values are explained in sec. 3.3.

Parameter	Value	Unit	Explanation
m	90	kg	Total mass
(x_g, y_g, z_g)	(0, 0, 0)	m	Centre of gravity in body reference frame
(x_{b0}, y_{b0}, z_{b0})	(0, 0, -0.18)	m	Centre of buoyancy in body reference frame
W	882.5895	N	Magnitude of gravity force
B	873.7636	N	Magnitude of buoyancy force
$\{a_{11} \ a_{22} \ a_{33} \ a_{44} \ a_{55} \ a_{66}\}$	{54 72 360 11 43.5 5.2}	kg	Added mass diagonal matrix
$\{d_{p11} \ d_{p22} \ d_{p33} \ d_{p44} \ d_{p55} \ d_{p66}\}$	{250 200 175 20 20 15}	$\frac{kg}{s}$	Linear potential damping diagonal matrix

7.7 Wake Model in MATLAB

This routine calculates the reduced velocity behind a cylindrical net, affected by current velocity



```

1  %*****
2  %   Subroutine wake_effect2D_multipleElements
3  %
4  %   Purpose: Top routine for calculaton of velocities through
5  %             and around a circular net.
6  %   Method: Mean turbulent wake velocites are calculated using
7  %             linearized turbulent wake equations at individual cylinders
8  %             that resemples the twines. Velocities in front of cage and
9  %             outside of cage are calculated using lagally's theorem.
10 %   Parameters
11 %   Input:
12 %       nu           - Kinematic viscosity
13 %       U_inf        - Uniform ambient velocity
14 %       Sn           - Solidity ratio
15 %       D_net        - Net diameter
16 %       d_tw         - Twine diameter
17 %       N_elements   - Number of screen elements
18 %       dx, dy       - Flow field spacial step length
19 %       xmin, xmax   - Flow field end coordinates in x-direction
20 %       ymin, ymax   - Flow field end coordinates in y-direction
21 %
22 %   Programmed by: Lars Haug
23 %   Date: September 2020
24 %*****
25 %% System properties
26
27 nu = 1e-6;
28 rho_s = 1025;
29 U_inf = 0.2;
30 Sn = 0.25;
31 D_net = 50;
32 d_tw = 0.0015;
33
34 Re = U_inf*d_tw/(nu*(1-Sn));
35
36 % Find meshsize of net based on a square-shaped knotless mesh
37 p = [Sn -2*d_tw d_tw^2];
38 l = roots(p);
39 [~,~,lambda] = find(l.*(l>d_tw)); % Choosing mesh size root larger than twine diameter
40
41 %% Discretization of flow field
42 N_elements = 16*10;
43 dx = D_net/50; dy = D_net/50;
44 xmin = -2*D_net;
45 xmax = 5*D_net;
46 ymax = 2*D_net;
47
48 % Flow field grid
49 x_vec = xmin:dx:xmax;
50 y_vec = -ymax:dy:ymax;
51 %% Discretization of screen elements
52 [x_nodes, y_nodes, lj, phi] = elementDiscretization(N_elements, D_net);
53 Ni = floor(lj/lambda);
54 N_cyl = Ni*N_elements;
55 [xi, yi] = sourcePointDiscretization(x_nodes, y_nodes, N_elements, Ni);
56 %% Calculation of inflow velocity on downstream net section
57 if Re < 10^(3/2)
58     C_D_cirCyl = 1 + 10/(Re^(2/3));
59 else
60     C_D_cirCyl = -78.46675 + 254.73873*log10(Re) - 327.8864*(log10(Re))^2 +
61         223.64557*(log10(Re))^3 - 87.92234*(log10(Re))^4 ...
62         + 20.00769*(log10(Re))^5 - 2.44894*(log10(Re))^6 + 0.12497*(log10(Re))^7;
63 end
64 cd = C_D_cirCyl*Sn*(2-Sn)/(2*(1-Sn)^2);
65 U_dnet = U_inf*(1-0.46*cd);
66 Re_dnet = U_dnet*d_tw/(nu*(1-Sn));
67 %% Memory Allocation
68 C_N = zeros(1, N_elements);
69 C_T = zeros(1, N_elements);
70 C_D = zeros(1, N_elements);
71 C_L = zeros(1, N_elements);
72 %% Coefficients

```

```

1  %*****
2  %   Subroutine sourcePointDiscretization
3  %
4  %   Purpose: Discretizes a circular cylinder into straight 2D
5  %             line elements.
6  %   Method:  Uniform radial spacing
7  %
8  %   Parameters
9  %   Input:
10 %   D_net      - Net diameter
11 %   N_elements - Number of elements
12 %
13 %   Output:
14 %   x_nodes, y_nodes - Vector of element coordinates
15 %   lj           - Element length (equal for all)
16 %   phi          - Angle relative to element normal vector and x-axis
17 %
18 %   Programmed by: Lars Haug
19 %   Date: September 2020
20 %*****
21
22 function [x_nodes, y_nodes, lj, phi] = elementDiscretization(N_elements, D_net)
23 N_nodes = N_elements+1;
24 dtheta = 2*pi/N_elements;
25 theta = [0:dtheta:N_elements*dtheta]-N_elements/2*dtheta/2;
26 [x_nodes, y_nodes] = pol2cart(theta, ones(1,N_nodes)*D_net/2);
27
28 lj = sqrt((x_nodes(end)-x_nodes(end-1))^2 + (y_nodes(end)-y_nodes(end-1))^2);
29
30 phi = zeros(1, N_elements);
31
32 for e = 1:N_elements
33     elem_centre_x = (x_nodes(e+1)+x_nodes(e))/2;
34     elem_centre_y = (y_nodes(e+1)+y_nodes(e))/2;
35
36     phi(e) = cart2pol(elem_centre_x,elem_centre_y);
37
38 end
39 end

```



```

1  %*****
2  %   Subroutine elementDiscretization
3  %
4  %   Purpose: Distributes source points along an element to represent
5  %             a twine.
6  %   Method:  Uniform radial spacing
7  %
8  %   Parameters
9  %   Input:
10 %   x_nodes, y_nodes - Vector of element coordinates
11 %   N_elements      - Number of elements
12 %   Ni              - Number of source points in single element
13 %
14 %   Output:
15 %   xi, yi         - Vector of source point coordinates
16 %
17 %   Programmed by: Lars Haug
18 %   Date: September 2020
19 %*****
20
21 function [xi, yi] = sourcePointDiscretization(x_nodes, y_nodes, N_elements, Ni)
22 % Memory Allocation
23 yi = zeros(1, N_elements*Ni);
24 xi = zeros(1, N_elements*Ni);
25
26 for e = 1:N_elements
27     lambda_x = (x_nodes(e+1)-x_nodes(e))/Ni;
28     lambda_y = (y_nodes(e+1)-y_nodes(e))/Ni;
29
30     if lambda_y == 0
31         yi(1,(e-1)*Ni+1:e*Ni) = y_nodes(e).*ones(1,Ni);
32     else
33         yi(1,(e-1)*Ni+1:e*Ni) =
34             y_nodes(e)+lambda_y/2:lambda_y:(y_nodes(e+1)-lambda_y/2);
35     end
36
37     if lambda_x == 0
38         xi(1,(e-1)*Ni+1:e*Ni) = x_nodes(e).*ones(1,Ni);
39     else
40         xi(1,(e-1)*Ni+1:e*Ni) =
41             x_nodes(e)+lambda_x/2:lambda_x:(x_nodes(e+1)-lambda_x/2);
42     end
43 end
end

```

```

1  %*****
2  %   Subroutine reynoldsDependentDragCoefficients
3  %
4  %   Purpose: Calculates drag coefficients of a screen.
5  %
6  %   Method: Extended screen model approach to fit experiments (Kristiansen,
7  %           Faltinsen, 2012).
8  %           Drag forces on net panel section is related to Sn, Re and phi.
9  %
10 %   Reference:
11 %           Kristiansen, T., Faltinsen, O.M., 2012. Modelling of current loads on
12 %           aquaculture net cages. Journal of Fluids and Structures 34, 218-235
13 %
14 %   Parameters
15 %   Input:
16 %   Re       - Reynoldsnumber of inflow on screen panel
17 %   Sn       - Solidity ratio of screen panel
18 %   phi      - Inflow attack angle
19 %
20 %   Output:
21 %   C_N      - Normal drag force coefficient
22 %   C_T      - Tangential drag force coefficient
23 %   C_D      - Drag force coefficient (parallell to flow)
24 %   C_L      - Lift force coefficient (perpendicular to flow)
25 %   cd       - Drag force coefficient at 0 deg attack angle
26 %   cl       - Oift force coefficient at 90 deg attack angle
27 %
28 %   Programmed by: Lars Haug
29 %   Date: September 2020
30 %*****
31 function [C_N, C_T, C_D, C_L, cd, cl] = reynoldsDependentDragCoefficients(Re, Sn,
32 phi)
33
34 phi = phi - pi*(phi<pi & phi>pi/2) + pi*(phi>-pi & phi<-pi/2);
35
36 if Re < 10^(3/2)
37     C_D_cirCyl = 1 + 10/(Re^(2/3));
38 else
39     C_D_cirCyl = -78.46675 + 254.73873*log10(Re) - 327.8864*(log10(Re))^2 +
40     223.64557*(log10(Re))^3 - 87.92234*(log10(Re))^4 ...
41     + 20.00769*(log10(Re))^5 - 2.44894*(log10(Re))^6 + 0.12497*(log10(Re))^7;
42 end
43
44 % Fourier Components
45 C_N_45 = C_D_cirCyl*Sn*(2-Sn)/(2*(1-Sn)^2)*(cos(pi/4))^2;
46 C_T_45 = pi/4*4*C_N_45/(8+C_N_45);
47 cd = C_D_cirCyl*Sn*(2-Sn)/(2*(1-Sn)^2);
48 cl = (0.5*cd-C_T_45)/sqrt(2);
49 a3 = 0.1;
50 a1 = 1-a3;
51 b4 = 0.1;
52 b2 = 1;
53
54 C_N = C_D_cirCyl*Sn*(2-Sn)/(2*(1-Sn)^2)*(cos(phi))^2;
55 C_T = phi^4*C_N/(8+C_N);
56 C_D = cd*(a1*cos(phi) + a3*cos(3*phi));
57 C_L = cl*(b2*sin(2*phi) + b4*sin(4*phi));
58 end

```

```

1  %*****
2  %   Subroutine wakeFlow
3  %
4  %   Purpose: Calculation of velocities in flow field
5  %
6  %   Method: Mean turbulent wake velocities are calculated using
7  %           linearized turbulent wake equations at individual cylinders
8  %           that resembles the twines. Velocities in front of cage and
9  %           outside of cage are calculated using lagally's theorem.
10 %   Parameters
11 %   Input:
12 %   rho_s       - Water density
13 %   U_dnet      - Inflow velocity of downstream net sections
14 %   U_inf       - Uniform ambient velocity
15 %   Sn          - Solidity ratio
16 %   D_net       - Net diameter
17 %   d_tw        - Twine diameter
18 %   N_elements  - Number of screen elements
19 %   C_D         - Vector of drag coefficients on screen elements
20 %   x_vec, y_vec - Elements coordinate
21 %   xi, yi      - Source points coordinate
22 %
23 %   Output:
24 %   u, v        - Velocitysssss
25 %
26 %   Programmed by: Lars Haug
27 %   Date: September 2020
28 %*****
29
30 function [u, v] = wakeFlow(U_dnet, D_net, N_elements, U_inf, rho_s, C_D, lj, x_vec,
31 y_vec, xi, yi, C_Di, d_tw, Ni, dy)
32 % Memory allocation
33 u_source = zeros(length(x_vec),length(y_vec));
34 v_source = zeros(length(x_vec),length(y_vec));
35
36 u1_sCyl = zeros(length(x_vec),length(y_vec));
37 u_sCyl = zeros(length(x_vec),length(y_vec));
38 inWake = zeros(length(x_vec),length(y_vec));
39 outWake = ones(length(x_vec),length(y_vec));
40
41 b = D_net/2;
42
43 U_elem = [ones(1,N_elements/2)*U_dnet ones(1,N_elements/2)*U_inf];
44 F_D = 0.5*rho_s.*U_elem.^2.*C_D*lj;
45
46 q_source = sum(F_D)/(rho_s*U_inf);
47
48 for k = 1:length(x_vec)
49     x = x_vec(k);
50     if x > 0
51         b = wakeWidth(b, C_Di, d_tw, x, xi, yi, Ni, N_elements, dy);
52         [th1, r1] = cart2pol(x,b);
53         u_source_boundary = U_inf + q_source/(2*pi*r1)*cos(th1);
54     end
55     for i = 1:length(y_vec)
56         y = y_vec(i);
57         [th1, r1] = cart2pol(x,y);
58
59         %Skip Calculations inside cage
60         if x^2+y^2 < (D_net/2)^2
61             continue
62         end
63
64         u_source(k,i) = U_inf + q_source/(2*pi*r1)*cos(th1);
65         v_source(k,i) = q_source/(2*pi*r1)*sin(th1);
66
67         if x > 0
68             [u_sCyl(k,i), inWake(k,i), outWake(k,i)] = CylModNetWake(x, y, xi, yi,
69                 C_Di, U_dnet, d_tw, Ni, N_elements, u_source_boundary, b);
70
71             u1_sCyl(k,i) = U_inf - u_sCyl(k,i);
72         end
73     end
74 end

```

